Loss of Ena/VASP interferes with lamellipodium architecture, motility and integrin-dependent adhesion

Julia Damiano-Guercio[1], Laëtitia Kurzawa[2,*], Jan Mueller[3,*], Georgi Dimchev[4,*], Maria Nemethova[3,*], Thomas Pokrant[1], Stefan Bruehmann[1], Joern Linkner[1], Laurent Blanchoin[2], Michael Sixt[3], Klemens Rottner[4,5] and Jan Faix[1]

[1]Institute for Biophysical Chemistry, Hannover Medical School, Carl-Neuberg-Str. 1, 30625 Hannover, Germany; [2]CytoMorphoLab, UMR5168, Integrative Structural and Cellular Biology Department, Interdisciplinary Research Institute of Grenoble, CEA, CNRS, INRA, Grenoble-Alpes Univ., 17 rue des Martyrs, 38054, Grenoble, France. [3]Institute of Science and Technology Austria (IST Austria), am Campus 1, 3400 Klosterneuburg, Austria; [4]Division of Molecular Cell Biology, Zoological Institute, Technical University Braunschweig, Spielmannstrasse 7, 38106 Braunschweig, Germany. [5]Molecular Cell Biology Group, Helmholtz Centre for Infection Research, Inhoffenstrasse 7, 38124 Braunschweig, Germany.

*These authors contributed equally to this work.

Send correspondences to:

Jan Faix

Phone: +49-511-532-2928

Fax: +49-511-532-5966

Email: faix.jan@mh-hannover.de

Abstract

Cell migration entails networks and bundles of actin filaments termed lamellipodia and microspikes or filopodia, respectively, as well as focal adhesions, all of which recruit Ena/VASP family members hitherto thought to antagonize efficient cell motility. However, we find these proteins to act as positive regulators of migration in different cell lines. CRISPR/Cas9-mediated loss of Ena/VASP proteins reduced lamellipodial actin assembly and perturbed lamellipodial architecture, as evidenced by changed network geometry as well as reduction of filament length and number that was accompanied by abnormal Arp2/3 complex and heterodimeric capping protein accumulation. Loss of Ena/VASP function also abolished the formation of microspikes normally embedded in lamellipodia, but not of filopodia capable of emanating without lamellipodia. Ena/VASP-deficiency also impaired integrin-mediated adhesion accompanied by reduced traction forces exerted through these structures. Our data thus uncover novel, cellular Ena/VASP functions of these actin polymerases that are fully consistent with their promotion of cell migration.

Introduction

Adhesion and migration are invariably driven by continuous and dynamic actin cytoskeleton remodeling (Blanchoin et al., 2014). The major protrusive structure of migrating cells on flat and rigid substrata is the sheet-like lamellipodium (Letort et al., 2015; Rottner et al., 2017). The extension of dense and branched actin filaments in the lamellipodium drives its growth and pushes the membrane forward (Koestler et al., 2008; Mullins et al., 1998; Pollard and Borisy, 2003; Vinzenz et al., 2012). Branching by Actin-related protein (Arp) 2/3 complex is activated by the WAVE regulatory complex (WRC) downstream of Rac subfamily GTPase signaling (Eden et al., 2002; Ismail et al., 2009; Molinie and Gautreau, 2018). Consistently, knockdown or knockout of essential Arp2/3 complex (Suraneni et al., 2012; Wu et al., 2012)

or WRC subunits (Innocenti et al., 2004; Schaks et al., 2018; Steffen et al., 2004) or Rac GTPases (Schaks et al., 2018; Steffen et al., 2013) all abrogated lamellipodium formation. The lateral flow of actin filaments and bundles embedded in the lamellipodium, called microspikes, is driven by actin assembly at the membrane (Oldenbourg et al., 2000). When microspikes transform and protrude beyond the lamellipodium edge, they are called filopodia (Small, 1988; Svitkina et al., 2003). Yet, in spite of both being built of parallel actin filament bundles and sharing constituents, filopodia and microspikes display important differences. As opposed to microspikes as integral parts of lamellipodial networks, filopodia can kink and bend (Nemethova et al., 2008), arising independently and even in excess in the absence of lamellipodia (Gupton et al., 2005; Koestler et al., 2013; Steffen et al., 2006; Wu et al., 2012). Consistently, filopodia can form around the entire cell periphery and at the dorsal surface (Block et al., 2008; Bohil et al., 2006; Pellegrin and Mellor, 2005). Moreover, rates of actin polymerization in microspikes and lamellipodia are indistinguishable from each other (Lai et al., 2008; Oldenbourg et al., 2000), whereas those in filopodia appear to be regulated independently.

Filament elongation is driven by formins and Ena/VASP proteins. Formins are dimeric multi domain proteins that remain tightly associated with growing filament barbed ends while accelerating their growth (Kovar et al., 2006). Several formins such as mDia2 (Block et al., 2008; Yang et al., 2007) and the formin-like family members 2 (FMNL2) and 3 (Block et al., 2012; Harris et al., 2010; Kage et al., 2017; Young et al., 2018) localize at lamellipodia and filopodia tips, and have been implicated in driving these protrusions and cell migration.

Ena/VASP family proteins localize to sites of active actin assembly including focal adhesions (FA) (Gertler et al., 1996; Reinhard et al., 1995), stress fibers (Gateva et al., 2014; Rottner et al., 2001), and lamellipodial or filopodial tips (Rottner et al., 1999; Svitkina et al., 2003). Vertebrates harbor Vasodilator-stimulated phosphoprotein (VASP), mammalian Enabled

(Mena), and Ena-VASP-like (Evl). All family members are tetramers encompassing domains allowing for interactions with FPPPP-containing proteins, actin monomers, profilin-actin complexes and actin filaments (Bear and Gertler, 2009). Ena/VASP tetramers are poorly processive, but processivity and resistance against heterodimeric capping protein that stops barbed end growth, increases markedly upon oligomerization or clustering (Breitsprecher et al., 2011a, 2008; Brühmann et al., 2017; Hansen and Mullins, 2015).

Genetic removal of all three Ena/VASP proteins was previously shown to abrogate filopodia formation in neuronal cells (Kwiatkowski et al., 2007). The functions of Ena/VASP proteins in cell motility have remained more controversial. Although VASP accumulation at lamellipodia tips positively correlates with protrusion rates (Rottner et al., 1999), genetic inactivation of VASP and Mena or mitochondrial Ena/VASP sequestration in fibroblasts was reported to increase cell migration (Bear et al., 2002, 2000). This phenotype was explained by lamellipodia protruding more persistently after interference with Ena/VASP function, and containing shorter and more branched filaments. Excess of Ena/VASP, in contrast, generated lamellipodia with longer, less branched filaments, prone to lifting rearwards during membrane ruffling, therefore driving migration less efficiently (Bear et al., 2002). Despite this negative role in fibroblast motility, the proposed positive regulatory function of Ena/VASP on lamellipodial filaments was consistent with their clear relevance in the motility of *Listeria* harboring the Ena/VASP ligand ActA (Geese et al., 2002; Loisel et al., 1999; Skoble et al., 2001). Whether the reported negative correlation of Ena/VASP activity with migration can be generalized, has remained unanswered.

Finally, although Ena/VASP proteins are prominent FA components, their roles in cell substrate adhesion and FA formation have also remained controversial. Both inhibitory (Galler et al., 2006) and stimulatory roles (Gupton et al., 2012; Kang et al., 2010; Puleo et al., 2019; Young and Higgs, 2018) on adhesion were reported, whereas one study did not detect

any effect in fibroblasts lacking Mena and VASP (Bear et al., 2000). To resolve these discrepancies, we characterized cells disrupted for individual, two or all three Ena/VASP family members in distinct types of parental cells, and explored the impact of their individual and collective removal on formation of different protrusion types, migration efficiency and adhesion.

Results

Loss of Ena/VASP impairs cell migration in B16-F1 cells

To evaluate the physiological function of Ena/VASP proteins in a rapidly migrating cell type, we sequentially inactivated the three Ena/VASP paralogues Evl, VASP and Mena using CRISPR/Cas9 technology in B16-F1 mouse melanoma cells. Respective protein loss in independent clonal cell lines was confirmed by immunoblotting and verified by sequencing of genomic target sites (***Figure 1A, Supplement 1***). Migration rates of B16-F1 wild-type and two independent lines of each genotype were then analyzed on laminin by phase-contrast, time-lapse microscopy. Interestingly, consecutive Ena/VASP member removal caused an increasing phenotype in migration rate, ranging from a comparably modest reduction of 1.25 ± 0.37 µm/min and 1.19 ± 0.47 µm/min for single Evl KO mutants (E-KO) as compared to control (1.44 ± 0.4 µm/min), to 0.62 ± 0.25 µm/min and 0.57 ± 0.27 µm/min in Evl and VASP double-KOs (EV-KO), and 0.47 ± 0.19 µm/min and 0.43 ± 0.22 µm/min in triple-KOs (EVM-KO) (***Figure 1B, Figure 1-video 1***). This was accompanied by a gradual increase in directionality culminating in EVM-KO cells that were 46% more directional as compared to wild-type B16-F1 (***Figure 1C***). Quantitative analyses of the turning angles revealed an incrementally increased frequency at 0° from 10.2% in wild-type to 12.3% in single KO, 16.1% in double KO and 16.9% in triple KO cells, in support of the higher directionality in mutant cells that coincided with their reduced motility (***Figure 1D***). Since independently

generated Ena/VASP mutant cell lines behaved highly similar in distinct assays, data derived from one triple-KO clone (#23.7.66) are shown below. To ensure that observed phenotypes were Ena/VASP-specific, the same parameters were analyzed in reconstituted EVM-KO mutant cells ectopically expressing EGFP-tagged VASP, Evl or Mena. Re-expression of VASP, which was found to contribute most efficiently to motility, largely rescued cell speed, directionality and frequency of turning angles (***Figure 1E-F, Figure 1-figure supplement 1A***). The rescue experiments with EGFP-tagged Evl or Mena yielded similar results, but these proteins were slightly less effective in restoring cell speed (***Figure 1E-F***). Finally, we calculated the mean square displacement (MSD) in wild-type and the entire collection of mutant cells to assess their effective directional movement. Despite their higher directionality, presumably owing to their considerably slower motility, all Ena/VASP mutant cells displayed incrementally decreasing and lower MSD values as compared to control (***Figure 1G***). Notably, in EVM-KO cells rescued with EGFP-tagged VASP, Evl or Mena, the MSD values were again markedly increased (***Figure 1-figure supplement 1B***).

Ena/VASP-deficiency consistently diminishes cell migration in fibroblasts

To corroborate our findings in strongly adherent cell types, we first examined MV^{D7} mouse embryonic fibroblasts. This cell line was described previously to derive from Mena/VASP-deficient mice and selected initially to lack detectable expression of Evl (Bear et al., 2000), albeit later stated to contain trace amounts (Auerbuch et al., 2003). We did confirm the absence of Mena and VASP in these cells by immunoblotting (***Figure 2A***). Surprisingly, however, our newly-generated antibodies raised against and affinity-purified with Evl (see Materials and Methods) now identified the protein at low, but clearly detectable levels in this cell line. Thus, to obtain fibroblasts devoid of all three Ena/VASP proteins, we employed CRISPR/Cas9 to eliminate Evl in MV^{D7} cells, with Evl disruption confirmed by

immunoblotting and sequencing as described for B16-F1 cells above (***Figure 2A, Supplement 1***). Since distinct triple-KO cell lines behaved again in a highly comparable fashion, only data from clone #31 referred to as MVE-KO are shown. We first analyzed migration on fibronectin by phase-contrast time-lapse imaging of MV^{D7} and MVE-KO as well as MVE-KO cells rescued with EGFP-tagged Evl. In MVE-KO, cell speed (0.41 ± 0.17 µm/min) was significantly reduced as compared to MV^{D7} control (0.56 ± 0.19 µm/min), whereas migration of MVE-KO cells expressing EGFP-Evl (0.68 ± 0.28 µm/min) was markedly increased (***Figure 2B***). Remarkably, in spite of their higher cell speed, MV^{D7} exhibited even lower MSD values than MVE-KO cells (***Figure 2C***), apparently caused by the lower directionality of the former, and as evidenced by their trajectories in radar plots (***Figure 2-figure supplement 1A-B***). As expected, triple-KO cells reconstituted with Evl displayed strongly increased MSD values (***Figure 2C***) and decreased directionality (***Figure 2-figure supplement 1A-B***).

Additionally, we analyzed directional cell migration of these cell lines in wound closure scratch assays (***Figure 2D***). Average wound closure rates were reduced by 24% in MVE-KO cells (18121 ± 2658 $\mu m^2 h^{-1}$) as compared to MV^{D7} cells (23906 ± 2042 $\mu m^2 h^{-1}$) (***Figure 2E***). Interestingly, reconstitution of MVE-KO cells with stable Evl expression significantly increased wound closure to rates virtually identical to MV^{D7} controls (***Figure 2F***). Thus, despite comparably low expression of Evl in MV^{D7} fibroblasts, its elimination caused clearly detectable impairment of cell migration.

To assess the contribution of the two other Ena/VASP family members in fibroblast motility, we also disrupted the genes encoding Mena and VASP individually or in combination in mouse NIH 3T3 fibroblasts by CRISPR/Cas9 technology, and again confirmed elimination of respective proteins by immunoblotting and sequencing (***Figure 2G***, ***Supplement 1***). Migration rates of NIH 3T3 wild-type and two independent lines of each genotype were then

again analyzed on fibronectin by phase-contrast time-lapse imaging. Comparable to the findings in B16-F1 cells, consecutive removal of Mena and VASP in NIH 3T3 cells also caused a step-wise increase in migration phenotype, ranging from a rather modest average reduction of about 10.6% for single Mena KO mutants (M-KO) to 31.6% in Mena and VASP double-KO (MV-KO) mutants as compared to control (***Figure 2H***). Consistently, these Ena/VASP mutant cells also exhibited incrementally decreasing and lower MSD values as compared to NIH 3T3 wild-type controls (***Figure 2I***). All these findings combined, strongly suggest, quite strikingly, that Ena/VASP proteins execute conserved and prominent, positive regulatory functions in cell migration, in a fashion irrespective of cell type (melanoma cells and fibroblast alike) and thus type of mesenchymal migration and/or signaling condition, as induced by extracellular matrices (laminin *versus* fibronectin).

To relate the specific contributions of individual Ena/VASP family members to cell migration, we finally determined the cellular concentrations of expressed orthologues in B16-F1, NIH 3T3 and MV^{D7} cells. For this, we titrated defined amounts of recombinant proteins with total cell lysates from a given number of cells in immunoblots, and calculated resulting absolute levels of each protein in the different cell types (***Figure 2J***). Interestingly, in spite of considerably higher expression of Mena in B16-F1 and NIH 3T3 cells as compared to VASP, and in particular relative to Evl, loss of Mena affected migration much less strongly than, for instance, removal of VASP. This suggests a certain differentiation of Ena/VASP family member function despite clearly overlapping functions.

Loss of Ena/VASP reduces lamellipodium width and abrogates microspike formation

Since migration is mainly driven by actin assembly in the lamellipodium, we then analyzed actin filament (F-actin) distribution in B16-F1 and EVM-KO cells after phalloidin staining. As opposed to B16-F1 control cells, which displayed prominent lamellipodia with numerous

microspikes, EVM-KO cells developed strongly compromised lamellipodia largely lacking microspikes (***Figure 3A, Figure 3-video 1***). Quantification of F-actin contents in lamellipodia revealed about 45% reduction in the triple mutant, and the average width of lamellipodia was diminished by about 65% to 0.8 ± 0.2 µm when compared to wild-type with 2.3 ± 0.7 µm. In mutant cells reconstituted with EGFP-VASP, F-actin intensity increased even 40% above wild-type levels, and lamellipodium width was readily restored to 2.7 ± 0.8 µm (***Figure 3B-C***). Similar, but less pronounced effects were found after rescue with EGFP-tagged Evl or Mena as compared to VASP (***Figure 3-figure supplement 1A-C***). Given the evident lack of microspikes, we stained for the actin-crosslinking protein fascin, a well-established constituent of microspikes in B16-F1 cells (Vignjevic et al., 2006). Again, the triple mutant virtually lacked fascin-containing bundles, as opposed to wild-type and reconstituted mutants expressing VASP, despite unchanged expression of fascin in the mutant (***Figure 3D-G***). This was corroborated by imaging of wild-type and EVM-KO cells expressing EGFP-fascin (**Figure 3-*video 2***). Finally, we examined the gene dose-dependent requirement for Ena/VASP family members in microspike formation and found that virtually complete loss of microspikes was observed only upon disruption of all three family members (***Figure 3H***).

Potent filopodia inducers fail to rescue microspike formation in Ena/VASP-deficient cells

We then asked whether microspikes can be reformed in the triple-mutant upon transient expression of potent factors known to induce peripheral protrusions, and in particular related protrusive structures such as filopodia (Block et al., 2008; Bohil et al., 2006; Kage et al., 2017; Pellegrin and Mellor, 2005). We also used all Ena/VASP members as controls. Evl and Mena both rescued canonical lamellipodia with microspikes in EVM-KO comparable to

VASP, with Mena forming microspikes above average length (***Figure 4A, Figure 4-figure supplement 1A-B***). Strikingly, none of the agents established previously to be capable of inducing filopodia formation, i.e. constitutively active variants of the small Rho GTPase Rif (L77), the formins mDia2 (mDia2ΔDAD), FMNL3 (E275) and to lesser extent FMNL2 (E272), or unconventional myosin X were able to restore microspike-containing lamellipodia, indicating that microspike formation requires more specific activities that are critically dependent on Ena/VASP function (***Figure 4A***).

To explore this potential molecular difference between microspikes and filopodia more directly, we induced filopodia in the absence of lamellipodia in B16-F1 and EVM-KO cells. Since it is commonly assumed that lamellipodia emerge by extension of Arp2/3 complex-generated, dendritic filament networks downstream of WRC and Rac signaling (Pollard, 2007; Schaks et al., 2018; Steffen et al., 2013; Wu et al., 2012), we inhibited Arp2/3 complex with high concentrations of CK666 in combination with cell seeding on low concentrations of laminin, which aided inhibitor-mediated suppression of lamellipodia formation in these conditions (data not shown). Analyses of phalloidin-stained cells revealed that albeit reduced in formation frequency per cell, filopodia formation was still possible in EVM-KO cells (66% compared to B16-F1 control on low laminin). This confirmed that Ena/VASP family can indeed contribute to filopodia formation, as previously observed in *D. discoideum* (Han et al., 2002). At the same time, these data also illustrated that filopodia can indeed form to significant extent without lamellipodia, e.g. upon inhibition of Arp2/3 complex and thus in the absence of microspikes (***Figure 4B-C***), in spite of the reduced frequencies of filopodia formation observed here. Conversely, however, induction of filopodia formation by expression of constitutive active mDia2 (Block et al., 2008; Yang et al., 2007) was virtually identical in the EVM-KO mutant as compared to B16-F1 cells (***Figure 4D-E***), supporting the view of multiple pathways leading to filopodium formation (Young et al., 2015).

Loss of Ena/VASP changes distribution of Arp2/3 complex and capping protein and affects lamellipodial dynamics

To explore if or how loss of Ena/VASP function affected Arp2/3 complex accumulation, we immunolabelled the cells for the Arp2/3 complex and found that it accumulated in a peripheral band much narrower than commonly observed in wild-type lamellipodia (reduced by 64%), but with roughly 75% higher intensity at the tips of mutant lamellipodia (***Figure 5A-C***). The mutant phenotype was again Ena/VASP-specific, since it was perfectly rescued by transient expression of EGFP-tagged VASP and Evl, and at least partly by Mena. More specifically, VASP was slightly more effective than Evl, and Mena was capable of mediating a statistically significant rescue only concerning width of observed Arp2/3 complex signal (***Figure 5A-C***, ***Figure 5-figure supplement 1A-C***). We also monitored the distributions of heterodimeric capping protein (CP), the F-actin binding protein cortactin and the WRC-subunit WAVE2. CP and cortactin distributions were highly reminiscent of changes in Arp2/3, again much narrower (reduced by 60% and 67%, respectively), and with approximately 75% and 60% increased intensities in EVM-KO as compared to controls (***Figure 5D-F***, ***Figure 5-figure supplement 1D-I***). Interestingly, we found no noticeable difference in distribution and intensity of WAVE2 in wild-type *versus* EVM-KO (***Figure 5-figure supplement 1J-L***). This together with reversion to or close to wild-type levels of Arp2/3 complex, CP and cortactin by EGFP-tagged Ena/VASP family members illustrated their impact on the lamellipodial Arp2/3 complex machinery downstream, and thus independent of its major lamellipodial activator, WRC.

Next, we asked whether or to which extent lamellipodia protrusion was affected. To this end, we recorded wild-type, EVM-KO and VASP-reconstituted cells randomly migrating on laminin, and determined respective protrusion rates by kymograph analyses (***Figure 5G-H***,

Figure 5-video 1). Quantification revealed lamellipodia protrusion to be reduced by 35% in EVM-KO cells as compared to control or EVM-KO rescued with EGFP-VASP (***Figure 5I***). Notably, despite reduced protrusion, lamellipodia persistence was at best slightly reduced in EVM-KO cells, but not in a statistically significant fashion (***Figure 5J***), confirming that protrusion effectivity can be readily uncoupled from persistence (Block et al., 2012; Kage et al., 2017).

Ena/VASP proteins are potent actin polymerases (Breitsprecher et al., 2011a, 2008; Hansen and Mullins, 2010), implying that these factors could affect dynamics of actin assembly in lamellipodia. To test this experimentally, we assessed lamellipodial actin network assembly rates in wild-type and EVM-KO cells (***Figure 5K***, ***Figure 5-video 2***). Lamellipodial actin network translocation was also reduced by about 22% in EVM-KO as compared to B16-F1 controls, suggesting that the effects on protrusion described above can be explained, at least in part, by reduced actin network polymerization (***Figure 5L***).

Loss of Ena/VASP deteriorates lamellipodium architecture

To gain quantitative insights into the ultrastructural details of lamellipodial architecture at the single filament level, we employed three-dimensional (3D) electron microscopy of negatively stained B16-F1 wild-type and EVM-KO samples, allowing computer-assisted tracing of single filaments in 3D space (Mueller et al., 2017; Winkler et al., 2012). Consistent with actin assembly in lamellipodia tips (Lai et al., 2008), filaments are oriented with their barbed ends facing the membrane (Narita et al., 2012). In analogy to recent work (Mueller et al., 2017), barbed ends were scored in digitalized tomograms as the ends of filaments proximal to the leading edge and pointed ends as those distal to the leading edge. Barbed ends either represent actively growing or capped filaments, whereas pointed ends designate Arp2/3 complex-generated branch sites, severed or debranched filaments. In contrast to lamellipodia

of wild-type cells, EVM-deficient lamellipodia contained much sparser and less organized filament networks (***Figure 6A***, ***Figure 6-video 1***), which is consistent with the F-actin stainings in Figure 3A-B. Consistently, assessment of actin filaments in the front region (within a ~1µm broad zone behind the edge) revealed considerably shorter filaments in the mutant (***Figure 6B***). Moreover, towards the interior of the lamellipodium, filament density in the EVM-mutant decreased noticeably faster as compared to control, while at the edge, barbed ends occurred in excess in the mutant (***Figure 6C***). Consistent with reduced filament lengths (***Figure 6B***) and increased Arp2/3 intensities at the edge of EVM-KO cells (***Figure A-B***), assessed pointed end densities were significantly above control values in particular within the first half micron of the edge (***Figure 6C***). Finally, although both control and mutant lamellipodia exhibited a wide array of filament angles abutting the protruding front, with a clear maximum around 90° relative to the edge (***Figure 6D***), the distribution of filament angles in EVM-deficient lamellipodia was distinct, with the 90° peak being clearly less prominent (17% lower than in control). Conversely, filament fractions with diagonal angles were about doubled compared to controls. These data suggest that reduced filament mass and disordered filament network geometry in the mutant are causative for reduced protrusion and network assembly.

Loss of Evl impairs cell spreading and FA formation

To assess Ena/VASP functions in adhesion, we first analyzed spreading of MV^{D7}, derived MVE-KO and reconstituted fibroblasts expressing EGFP-Evl on fibronectin by time-lapse imaging (***Figure 7A, Figure 7-video 1***). Notably, MVE-KO cells displayed a substantial spreading defect that was fully rescued by Evl re-expression (***Figure 7B-C***). Consistent with the removal of Evl in MV^{D7} fibroblasts, B16-F1-derived EVM-KO cells also spread considerably slower than wild-type or reconstituted mutant cells expressing EGFP-tagged

VASP or Evl (***Figure 7-figure supplement 1A-B***). In these experiments, Evl rescued more effectively compared to VASP (***Figure 7-figure supplement 1C***). Then, we examined FA morphologies in MVE-KO fibroblasts expressing different Ena/VASP family members fused to EGFP. Untransfected MVE-KO cells formed noticeably smaller FAs on average than the same cells expressing distinct Ena/VASP family members, but again, the rescue with Evl appeared most effective (***Figure 7D***). To explore potential effects of Ena/VASP proteins on FA formation more systematically, MV^{D7}, MVE-KO and reconstituted cell lines migrating on fibronectin were labelled for the FA-marker protein vinculin and assessed for various features (***Figure 7E***). Images captured at identical settings were processed by a web-based FA analysis tool (Berginski and Gomez, 2013), allowing a global and unbiased assessment of multiple parameters. Consistent with previous work, untransfected MV^{D7} double-mutant cells still contained prominent FAs (Bear et al., 2000). Notably however, vinculin intensity was clearly reduced in the triple mutant by almost 30% as compared to the parental MV^{D7} cell line, and again fully rescued by Evl expression, while rescue of MVE-KO cells with VASP or Mena was less effective (***Figure 7F***). Consistently, FA size in MVE-KO cells was reduced by 18% as compared to MV^{D7} cells (***Figure 7G***), despite the low abundance of Evl in this cell line (***Figure 2J***). Furthermore, expression of VASP or Mena in MVE-KO cells increased FA size only by 11% or 16%, respectively, while expression of Evl increased FA size by more than 24%. Accordingly, Evl expression was most efficient in rescuing the average number of FAs per cell as compared to VASP and Mena (***Figure 7H***). Together, despite clearly overlapping functions of Ena/VASP proteins in various actin-dependent processes, Evl appeared more critical in the regulation of focal adhesions than VASP or Mena.

Loss of Evl diminishes generation of traction forces

Since Evl proved most effective in rescuing parameters addressing FA properties, we finally explored the functional consequence of Evl function in traction force development. To compare traction forces exerted onto a polyacrylamide substratum independently of cell size and geometry, MV^{D7}, MVE-KO cells, and reconstituted cells expressing EGFP-Evl were grown on top of crossbow-shaped micropatterns coated with fibronectin (Vignaud et al., 2014) (***Figure 8A***). Interestingly, the contractile energy was significantly reduced in MVE-KO cells as compared to MV^{D7} (***Figure 8B-C***), and rescued upon stable expression of EGFP-tagged Evl (***Figure 8D-E***). Moreover, the contractile energies of Evl-rescued MVE-KO and parental MV^{D7} cells were highly similar to each other. Comparable results were obtained with unconfined cells, i.e. homogenous fibronectin coating on polyacrylamide substrata, and thus in the absence of size- and geometry-specific constrains (***Figure 8-figure supplement 1A-B***).

Discussion

In contrast to earlier studies (Bear et al., 2002, 2000), we show that Ena/VASP actin polymerases positively regulate cell migration, since their consecutive loss in B16-F1 cells results in cumulative, reconstitutable motility phenotypes. Thus, despite increased directionality, the reduced net cell translocation rates observed in EVM-KOs as compared to wild-type occur because of reduced lamellipodial actin assembly and protrusion rates. Diminished migration was also observed in MV^{D7} fibroblasts after genetic removal of Evl as well as in NIH 3T3 fibroblast after consecutive disruption of Mena and VASP, supporting the view that Ena/VASP operate in a mechanistically conserved fashion, reconciling previous controversies (Auerbuch et al., 2003; Geese et al., 2002; Loisel et al., 1999; Rottner et al., 1999). But how can these discrepancies be explained? Firstly, MV^{D7} cells proved to be an excellent tool in the field for over two decades now, but were largely considered to be Ena/VASP-free, which we here show not to be the case. Secondly, the concept of Ena/VASP-

proteins antagonizing efficient cell motility in fibroblasts was largely developed further by inactivating these proteins in Rat2 cells through mitochondrial sequestration *versus* activating them through CAAX-mediating targeting to the plasma membrane (Bear et al., 2002). It was clearly shown in previous studies that mitochondrial sequestration of actin-binding proteins can co-recruit multiple additional interactors of such factors (Fradelizi et al., 2001), so the specificity of this approach for Ena/VASP proteins might be worth reconsidering. Furthermore, it is certainly worth noting that targeting through the general, isoprenylation-prone motif derived from small GTPases, the so called CAAX-box, is a very efficient means of targeting proteins to plasma membranes, but those membranes cannot be equalized to physiological accumulation of Ena/VASP proteins at the membrane, such as focal adhesions as well as tips of lamellipodia and filopodia (Rottner et al, 1999; Svitkina et al., 2003). In this respect, we should emphasize not to question the experimental outcome of previously published data. We should rather emphasize instead that previously employed approaches cannot be directly compared to the loss of function approaches developed here.

In line with markedly diminished migration, EVM-KO cells display aberrant, narrow lamellipodia with reduced F-actin densities, shorter filaments and perturbed network geometry. Nevertheless, we should stress the fact that for many years, it had remained unclear in the community whether or not Ena/VASP proteins were essential for the formation of lamellipodial actin networks, which we are clearly able to clarify here not to be the case. But what are the precise consequences of loss of Ena/VASP activity in those lamellipodia still formed in their absence? Interestingly, lamellipodial accumulation of Arp2/3 complex, CP and cortactin is markedly enhanced upon Ena/VASP removal. While CP and cortactin localization frequently coincides with Arp2/3 complex, the latter has indeed already been observed to be negatively correlated with Ena/VASP function (Samarin et al., 2003). Thus, it is tempting to speculate that loss of processive filament elongation upon Ena/VASP removal

can also increase capping of filaments and Arp2/3 complex-mediated, lamellipodial branching activity (Samarin et al., 2003). This would also be consistent with shorter and more highly branched filaments observed by platinum replica EM upon mitochondrial Ena/VASP sequestration (Bear et al., 2002). Future cryo-EM tomography studies will be required to assess in 3D to what extent increased Arp2/3 complex intensities found in EVM-KOs indeed correlate with enhanced branching.

Nevertheless, EVM-KO cells are still capable of impaired lamellipodia formation and migration, raising the question of alternative actin polymerases partly taking over. Previous studies have implicated formins in lamellipodia protrusion in B16-F1, including mDia2 (Yang et al., 2007) and FMNL 2 and -3 (Kage et al., 2017). Indeed, FMNL2/3 removal caused defects partly reminiscent of what's seen here, at least concerning impact on lamellipodial protrusion, actin filament densities or microspike formation (see below), although phenotypes seen upon Ena/VASP deficiency were much more severe. Thus, the extent of potential redundancy between all these factors will only be revealed by systematic, combinatorial loss of function studies and side-by-side, phenotypic comparison (Young et al., 2018). Derived conclusions will also have to consider the exciting, recently discovered 'distributive polymerase' activity ascribed to WAVE (Bieling et al., 2018).

As yet, authors of even highly relevant literature have decided not to clearly distinguish between filopodia and microspikes to facilitate analyses of finger-like protrusions (Svitkina et al., 2003; Vignjevic et al., 2006). However, the virtual absence of microspikes, but not of filopodia, in EVM-KO cells combined with the inability of established filopodia inducers such as mDia2, FMNL3, Myosin X and Rif to rescue microspikes clearly establishes, perhaps for the first time fundamental differences between these molecular entities. The mechanisms underlying filopodia assembly are still under debate: In the convergent elongation model, filopodia form by coalescence of lamellipodial filaments (Svitkina et al., 2003), whereas the

425 *de novo* nucleation model proposes filopodia to arise independently of lamellipodial actin
426 networks, as effected by formin-mediated filament nucleation and elongation (Faix et al.,
427 2009; Mellor, 2010). The findings provided here strongly suggest that in contrast to filopodia,
428 microspikes form exclusively by convergent elongation, as previously suggested (Svitkina et
429 al., 2003), whereas filopodia may emerge by multiple, distinct mechanisms (Young et al.,
430 2015), resolving a long-standing controversy in the field.
431 Ena/VASP proteins are well established to accumulate in FAs of adherent cells, and known to
432 reside in the force transduction layer in-between talin and ends of stress fiber filaments
433 (Kanchanawong et al., 2010). However, the presence of multiple orthologues and analyses of
434 only partially-depleted cells hitherto prevented careful functional assessment of their precise
435 contributions to integrin-dependent adhesion. Here we show that lack of Ena/VASP proteins
436 consistently impairs integrin-dependent spreading and changes in FA patterns. Moreover,
437 reduction of adhesion size and adhesion component intensity observed in fibroblasts well
438 correlates with diminished traction forces upon Ena/VASP protein disruption. This clearly
439 illustrates the positive regulatory function of Ena/VASP family members in adhesion
440 formation and exertion of traction forces onto the substratum. The particularly important role
441 of Evl in integrin-dependent adhesion is consistent with very recent work showing its specific
442 requirement for FA maturation, cell-matrix adhesion and mechanosensing (Puleo et al.,
443 2019).
444 Finally, we have not only sought to interpret all our phenotypes in the context of various
445 combinations of gene deletions employing up to three distinct cell types, but also assessed
446 their expression levels in different cell types relative to each other, which certainly adds an
447 additional layer of complexity. Two major points worth being more systematically followed
448 in the future are worth mentioning here. First, Mena is by far the most abundant protein
449 present in both melanoma and fibroblast cell lines, but in particular considering this fact,

phenotypes generated by its depletion are comparably modest. In spite of its abundance, we are tempted to speculate therefore that it simply does not sufficiently find its relevant, specific interactors that might promote its impact in other structures such as cell-cell contacts (Scott et al., 2006) or tissues like the nervous system (Kwiatkowski et al., 2007). Finally, given their comparably low abundance, VASP, and in particular Evl, are displaying surprisingly significant relevance in lamellipodia protrusion and adhesion formation, respectively, the molecular nature of which also remains to uncovered in future projects.

Materials and methods

Constructs

cDNAs encoding murine VASP (isoform 1), Mena (isoform 2), and Evl (isoform 2) were amplified by PCR from a NIH 3T3 cDNA library and ligated into suitable sites of pEGFP-C1 (Clontech, Palo Alto, CA). VASP cDNA was additionally inserted into the BglII and SalI sites of pmCherry (Addgene ID: 632524). For generation of stably transfected cell lines, the 1.3 kb Puro cassette was amplified by PCR using pPur (Clontech) as template and inserted into the Asp718 and BamHI sites of pEGFP-C1 to yield pEGFP-C1 Puro. Subsequently, the cDNA fragment encoding Evl was inserted into the BspEI and XhoI sites of pEGFP-C1 Puro. For generation of constitutively active murine mDia2 (Drf3) lacking the C-terminal regulatory DAD domain (1-1.036), the corresponding cDNA fragment was amplified from a NIH 3T3 cDNA library and inserted into the BspEI and Asp718 sites of pEGFP-C1. Plasmids pEGFP-C1 Lifeact-EGFP (Riedl et al., 2008), pEGFP-Rif-L77 (Aspenström et al., 2004), pEGFP-MyoX (Berg and Cheney, 2002), EGFP-FMNL2-E272 and EGFP-FMNL3-E275 (Kage et al., 2017) and pEGFP-fascin (Adams and Schwartz, 2000) have been described. pEGFP-βActin was from Clontech. For generation of recombinant antigens, respective sequences encoding for murine Evl (1-414), VASP (1-375), Mena (1-241), and WAVE2-

WCA (419-497) were amplified from plasmid DNA and inserted into BamHI/SalI sites of pGEX-6P-1 (GE Healthcare, Munich, Germany). Plasmids pGEX-6P-2-cortactin (Lai et al., 2009) and pGEX-6P-1-fascin (Breitsprecher et al., 2011b) have been described. Fidelity of generated plasmids was confirmed by sequencing.

Cell culture and transfection

B16-F1 mouse melanoma cells (CRL-6323) and mouse embryonic NIH 3T3 fibroblast (CRL-1658) were purchased from ATCC. The mouse embryonic fibroblasts cell line MV^{D7}, which expresses a temperature-sensitive version of large T antigen, was derived from Mena/VASP-deficient mice (Bear et al., 2000). For this study, MV^{D7} cells were additionally immortalized with a SV40 wild-type variant of large T antigen-transducing retrovirus by standard procedures, to allow cultivation at 37°C. Expression of Evl in original and derived MV^{D7} cells, immortalized with SV40 wild-type large T antigen, was not affected as assessed by immunoblotting (data not shown). B16-F1, NIH 3T3 and immortalized MV^{D7} cells were cultured at 37°C and 5% CO_2 in high glucose DMEM culture medium (Lonza, Cologne, Germany) supplemented with 10% FBS (Biowest), 2 mM UltraGlutamine (Lonza) and 1% Penicillin-Streptomycin (Biowest). B16-F1 cells were transfected with 1 µg plasmid DNA and MV^{D7} and NIH 3T3 cells with 3 µg plasmid DNA, respectively using JetPRIME transfection reagent (PolyPlus, Illkirch, France) in 35 mm diameter wells (Sarstedt, Nümbrecht, Germany) according to the manufacturer's protocol. Absence of mycoplasma in cell lines was routinely checked by the VenorGeM Mycoplasma Detection Kit (Sigma, St. Louis, MO).

Genome editing by CRISPR/Cas9

DNA target sequences were pasted into CRISPR/Cas9 design tool (http://crispr.mit.edu/) to generate sgRNAs of 20 nucleotides with high efficiency scores. In case of Evl, the targeting sequence 5'-GATCGGTACCCACTTCTTAC-3' was used to cover all possible splice variants. Accordingly, genome editing of VASP was performed with 5'-GTAGATCTGGACGCGGCTGA-3', and for disruption of Mena expression, the sgRNA 5'-AAGGGAGCACGTGGAGCGGC-3' was used. Respective sequences were ligated into expression plasmid pSpCas9(BB)-2A-Puro(PX459)V2.0 (Addgene plasmid ID: 62988) using BbsI (Ran et al., 2013). Validation of CRISPR construct sequences was performed using a 5'-GGACTATCATATGCTTACCG-3' sequencing primer. 24 h after transfection with the CRISPR constructs, cells were selected in culture medium containing puromycin (B16-F1: 2 µg/mL, MV^{D7}: 4 µg/mL and NIH 3T3: 5 µg/mL) for 4 days, and then cultivated for 24 h in the absence of puromycin. For isolation of clonal knockout cell lines, single cells were seeded by visual inspection into 96 well microtiter plates and expanded in pre-conditioned culture medium containing 20% BriClone supplement (NICB, Dublin City University, Ireland). Clones were analyzed by the TIDE sequence trace decomposition web tool (https://tide.deskgen.com/, (Brinkman et al., 2014)) and immunoblotting using specific antibodies, and subsequently verified by sequencing (***Supplementary file 1***). For the latter, respective DNA fragments of about 500 bp encompassing the target sites were first amplified from genomic DNA using the Evl primer combination 5'-AAGCCATGAGTCTCCCAAGC-3' and 5'-GTCTCACGCTTTGGCTCTCA-3', the VASP primer combination 5'-GTGTGGCCTGCCTATCTGTT-3' and 5'-CAGAGGGACAGAGGGACAGA-3', and the Mena primer pair 5'-TCAGGCAACTGCAAGAACAG-3' and 5'-CATCTCGGCTGTAGGAGGTG-3'. Subsequently, amplified fragments were inserted into pJet1.2 vector (Thermo Fisher Scientific, Carlsbad, CA) and used for transformation of *E.*

coli host DH5α (Thermo Fisher Scientific). At least 30 sequences were analyzed for each knockout clone.

Generation of recombinant proteins and antibodies

For expression of recombinant proteins, the *E. coli* strain Rossetta 2 (Novagen) was used. Expression of GST-tagged fusion proteins was induced using 1 mM isopropyl-ß-D-thiogalactoside (IPTG) (Carl Roth, Karlsruhe, Germany) at 21°C for 14 h. Purification of respective proteins from bacterial extracts was performed by affinity chromatography using Protino glutathione-conjugated agarose 4B (Macherey-Nagel, Düren, Germany). Except for GST-WAVE2-WCA, the GST-tag was removed by proteolytic cleavage with PreScission Protease (GE Healthcare), followed by a final polishing step of the proteins by size-exclusion chromatography on an Äkta Purifier System using either HiLoad 26/600 Superdex 200 or HiLoad 26/75 Superdex columns (GE Healthcare). Purified proteins were dialyzed against immunization buffer (150 mM NaCl, 1 mM dithiothreitol (DTT), and 20 mM Tris/HCl pH 7.4) and stored in aliquots at -20°C. Polyclonal antibodies against Evl, VASP, Mena, cortactin and WAVE2 were raised by immunizing New Zealand white rabbits with respective recombinant proteins following standard procedures. Evl, Mena and cortactin polyclonal antibodies were subsequently purified by affinity chromatography using antigens conjugated to sepharose. GST antibodies in the anti GST-WAVE2-WCA serum were absorbed by GST-affinity chromatography. Monoclonal antibodies against fascin were produced upon injecting recombinant fascin mixed with CpG-DNA as adjuvant (*Magic Mouse*, Creative, NY, USA) into 7 week-old, female mice (Charles River, USA) using standard hybridoma technology and antibody screening procedures in the PROCOMPAS graduate programme-funded monoclonal antibody facility (Braunschweig Integrated Centre of Systems Biology - BRICS,

Technische Universität Braunschweig). Hybridoma clone 5E2 was selected and kindly provided by Sabine Buchmeier and Prof. Dr. em. Brigitte Jockusch (TU Braunschweig).

Antibodies used

Immunoblotting was performed according to standard protocols using rabbit polyclonal antibodies directed against Evl (1:1000 dilution), VASP (1:1000 dilution), Mena (1:1000 dilution), WAVE2 (1:1000 dilution), GFP (1:2000) (Faix et al., 2001) or mouse monoclonal antibody against glyceraldehyde-3-phosphate dehydrogenase (GAPDH) (1:1000; #CB1001-500UG, Merck (Darmstadt, Germany)) and anti-fascin antibody 5E2 (undiluted hybridoma supernatant). Primary antibodies in immunoblots were visualized using phosphatase-coupled anti-mouse (1:1,000 dilution; #115-055-62, Dianova (Hamburg, Germany)) or anti-rabbit antibodies (1:1,000 dilution; #115-055-144, Dianova). For immunofluorescence, the following primary antibodies were used: rabbit anti-cortactin antibodies (1:1000 dilution), mouse monoclonal anti-fascin antibody 5E2 (undiluted hybridoma supernatant), mouse monoclonal anti-ArpC5A (p16-ArcA) from hybridoma culture clone 323H3 (Olazabal et al., 2002), mouse monoclonal anti-capping protein α1/α2 subunits (hybridoma supernatant; 1:4 dilution; Developmental Hybridoma Bank, University of Iowa, Iowa City, IA) and mouse monoclonal anti-vinculin antibody (1:1,000 dilution, #V9131, clone hVIN-1, Sigma). Primary antibodies were visualized in immunohistochemistry with polyclonal Alexa-555-conjugated goat-anti-rabbit (1:1,000 dilution; #A21429, Invitrogen (Carlsbad, CA)) or goat-anti-mouse (1:1,000 dilution, #A32727, Invitrogen) and Alexa-488-conjugated goat-anti-rabbit (1:1,000 dilution; #A-11034, Invitrogen) or goat-anti-mouse antibodies (1:1,000 dilution; #A-11029, Invitrogen). To enhance EGFP signals, Alexa488-conjugated nanobodies from Chromotek (Chromotek, (Planegg-Martinsried, Germany)) (1:200 dilution; #gba488)

were used. Atto550-phalloidin (1:250 dilution, #AD 550-82, Atto-Tec (Siegen, Germany)) was used for visualization of F-actin.

Immunoblotting

For preparation of total cell lysates, cells were cultured to confluency and trypsinized. Cell pellets were washed twice with cold PBS and lysed with cold RIPA buffer (150 mM NaCl, 1.0% Triton X-100, 0.5% sodium deoxycholate, 0.1% sodium dodecyl sulfate (SDS), 50 mM Tris, pH 8.0) supplemented 5 mM benzamidine (Carl Roth), 0.1 mM AEBSF (AppliChem, Darmstadt, Germany) and Benzonase (1:1000, Merck) for 1 h at 4°C on a wheel rotator. Cell lysates were subsequently homogenized by passing the lysate 10 times through a syringe cannula (Braun). Protein contents of total cell lysates were determined by Pierce BCA assay (Thermo Fisher Scientific) using a Synergy 4 fluorescence microplate reader (Biotek, Bad Friedrichshall, Germany) according to manufacturer's protocol. 50 µg (B16-F1) or 100 µg (MEF) of total proteins per lane were subjected to SDS-PAGE, and transferred by semi-dry blotting onto nitrocellulose membranes (Hypermol, Hannover, Germany). Blotting membranes were then blocked with NCP buffer (10 mM Tris/HCL, 150 mM NaCl, 0.05% Tween-20, 0.02% NaN_3, pH 8.0,) containing 4% bovine serum albumin (BSA) for 1 h and incubated with primary antibodies overnight in the same buffer. After extensive washing of membranes and incubation with secondary, phosphatase-conjugated antibodies for at least 2 hours, blots were developed with 20 mg/mL of 5-brom-4-chlor-3-indolylphosphat-p-toluidin (BCIP) in $NaHCO_3$, pH 10.0.

Quantification of cellular Ena/VASP protein concentrations

Total cellular concentrations of Ena/VASP family members in used cell lines were quantified from immunoblots using orthologue-specific antibodies by titrating total cell lysates

596 corresponding to a defined number of B16-F1, NIH 3T3 and MVD7 cells with dilution series
597 containing defined amounts of recombinant proteins loaded on the same gels. Band
598 intensities were quantified by ImageJ software. The cell volume for each cell type was
599 calculated from phase-contrast images of freshly trypsinized, non-adherent cells (>50 for
600 each cell line). The volume of the nucleus was subtracted from the cell volume to obtain the
601 volume of the cytoplasm.
602
603 **Live cell imaging**
604 Time-lapse imaging of cells was performed using an Olympus XI-81 inverted microscope
605 (Olympus, Hamburg, Germany) driven by Metamorph software (Molecular Devices, San
606 Jose, CA) and equipped with objectives specified below and a CoolSnap EZ camera
607 (Photometrics, Photometrics, Tucson, AZ). Cells were seeded onto 35 mm glass bottom
608 dishes (Ibidi, Planegg-Martinsried, Germany) coated with either 25 µg/mL laminin (Sigma)
609 in case of B16-F1 cells and derived clones, or with 10 µg/mL fibronectin (Roche, Penzberg,
610 Germany) in case of MV^{D7}, NIH 3T3 and their derivatives, and maintained in imaging
611 medium composed of F-12 Ham Nutrient Mixture with 25 mM HEPES (Sigma), the latter to
612 compensate for the lack of CO_2, and supplemented with 10% FBS (Biowest, Nuaillé, France),
613 1% Penicillin-Streptomycin (Biowest), 2 mM stable L-glutamine (Biowest), and 2.7 g/L D-
614 glucose (Carl Roth) in an Ibidi Heating System at 37 °C. For random motility assays, B16-
615 F1cells were seeded at low density onto the dishes and allowed to adhere for 3 h.
616 Subsequently, the medium was exchanged with imaging medium, the chamber mounted into
617 a heating system, and cells recorded by time-lapse phase-contrast imaging at 60 sec intervals
618 for 3 h using an Uplan FL N 4x/0.13NA objective (Olympus). NIH 3T3, MV^{D7} and derived
619 cells were allowed to settle for 6 h after seeding and imaged at 10 min intervals for 10 h using
620 an UPlan FL N 10x/0.30NA objective (Olympus). Single cell tracking was performed in

ImageJ by MTrackJ. Analyses of cell speed and cell trajectories, turning angles, and mean square displacements were performed in Excel (Microsoft, Redmond, WA) using a customized macro (Litschko et al., 2018). Cells that contacted each other or divided were excluded from analyses. Directionality index ratio was determined by dividing the shortest distance between starting and end points (d) by the actual trajectories (D). For wound healing assays, MV^{D7} cells were seeded onto uncoated dishes and expanded to confluency. Subsequently, the monolayer was scratched with a 200 µL pipette tip, the cells washed three times with warm imaging medium, and recorded by phase-contrast time-lapse imaging at 10 min intervals for 20 h using an UPlan FL N 10x/0.30NA objective (Olympus). Wound closure rates were determined in ImageJ by measuring decrease of scratch area over time. Lamellipodial protrusions were recorded at 5 sec intervals for 10 min using an UPlan FL 40x/0.75NA objective (Olympus). Protrusion rates of advancing lamellipodia assessed over a time period of 2.5 min were quantified by first generating kymographs from time-lapse movies of the cell periphery using ImageJ, followed by slope determination from these kymographs. Lamellipodial persistence of randomly migrating B16-F1 and derived cells on laminin was determined by phase-contrast time-lapse microscopy using an UPlan FL N 10x/0.30NA objective and a frame rate of 1 frame per minute. Lamellipodial persistence was defined as time in min from initiation till collapse of the lamellipodium. Spreading of B16-F1 and derived clones was monitored at 30 sec intervals by time-lapse phase-contrast imaging for 30 min using an UPlan FL N 10x/0.30NA objective immediately after seeding, and spreading of MV^{D7} and derived lines were imaged at 30 sec intervals for 1 h using an Olympus LUCPlan FL N 20x/0.45NA objective. Quantification of cell spreading was executed with ImageJ from time-lapse movies by measuring increase of cell area over time. For epifluorescence imaging of fluorescently-labelled cells, B16-F1, EVM-KO and reconstituted EVM-KO cells expressing mCherry-VASP were transfected with either

pEGFP-Lifeact or pEGFP-fascin. 24 h post transfection, cells were seeded into imaging medium, and after 3 h, migrating cells recorded by time-lapse imaging at 10 sec intervals for 10 min using an Olympus 40x/0.75NA Uplan FL objective. In motility and spreading assays, reconstituted cells expressing EGFP-tagged VASP, Evl or Mena were identified by epifluorescence imaging.

Immunofluorescence

If not indicated otherwise for immunofluorescence labelling, cells were fixed in pre-warmed, 4% PFA in PBS, pH 7.3 for 20 min, subsequently washed three times with PBS supplemented with 100mM glycine, permeabilized with 0.1% Triton X-100 in PBS for 3 min and blocked in PBG (PBS, 0.045% cold fish gelatin (Sigma), and 0.5% BSA). For immunolabeling with fascin, cells were fixed in -20°C cold methanol. For immunolabeling of capping protein, the cells were fixed with 3% glyoxal at pH 5.0 as described (Richter et al., 2018) and then treated as above. To reduce cytoplasmic background in vinculin stainings, cells were fixed for 1 min with 2% PFA in PBS containing 0.3% Triton X-100 and then postfixed with 4% PFA in PBS for 20 min as described (Kage et al., 2017). Primary antibodies were incubated overnight, followed by extensive washing of the specimens with PBG and incubation with respective secondary antibodies for at least 2 h. GFP signals were enhanced with Alexa488-conjugated nanobodies. F-actin was visualized with Atto550 phalloidin. Imaging of fixed cells was performed with an Olympus XI-81 inverted microscope equipped with an UPlan FI 100x/1.30NA oil immersion objective or an LSM510 Meta confocal microscope (Carl Zeiss, Jena, Germany) equipped with a Plan-Neofluar 63x/1.3NA oil immersion objective using 488 nm and 543 nm laser lines.

Fluorescence intensities of phalloidin or lamellipodial proteins were measured from still images captured at identical settings using ImageJ software after background subtraction.

Mean pixel intensities in lamellipodial regions of interest are shown as whiskers-box plots including all data points.

Induction of filopodia in absence of lamellipodia

B16-F1 wild-type and EVM-KO cells were seeded onto low laminin (1µg/mL) for 1 h, a concentration lower than the threshold for inducing prominent lamellipodia in this cell type and conditions (data not shown). Then, the cells were incubated for 2 h with the Arp2/3 complex inhibitor CK666 (200 µM) to completely abolish lamellipodia and trigger filopodia formation. Subsequently, cells were fixed and stained with phalloidin for the actin cytoskeleton followed by confocal imaging.

Determination of actin assembly rates in lamellipodia

Quantification of lamellipodial actin polymerization rates were performed in B16-F1 and EMV-KO cells transiently expressing EGFP-ß-actin, by photobleaching protruding lamellipodial regions and subsequently measuring the distance of fluorescence recovery from the lamellipodium tip over time, essentially as described (Dimchev and Rottner, 2018). In brief, photobleaching of EGFP-ß-actin was accomplished on an epi-FRAP system, equipped with a 405-nm diode laser (settings: 65 mW laser power, 10-pixel laser beam diameter, 1ms bleach dwell time/pixel), which was manually triggered in selected regions during image acquisition (exposure time of 500 ms). Time-lapse imaging was performed with an interval of 1.5 sec between frames. Images were acquired with a 100x/1.4NA Plan apochromatic oil immersion objective on an inverted Axio Observer (Carl Zeiss, Jena, Germany) using a DG4 light source (Sutter Instrument, Novato, CA) for epifluorescence illumination and a CoolSnap-HQ2 camera (Photometrics, Tucson, AZ), driven by VisiView software (Visitron Systems, Puchheim, Germany).

696

697 **Electron tomography**

698 B16-F1 and EMV-KO cells were grown on Formvar-coated copper-palladium grids coated
699 with 25 µg/mL laminin (Sigma) in laminin coating buffer (150 mM NaCl, 50 mM Tris, pH
700 7.5). The cells were simultaneously extracted and fixed for 1 min with 0.5% Triton X-100
701 (Fluka, Buchs, Switzerland) and 0.25% glutaraldehyde (Agar Scientific, Stansted, United
702 Kingdom) in cytoskeleton buffer (10 mM MES buffer, 150 mM NaCl, 5 mM EGTA, 5 mM
703 glucose and 5 mM $MgCl_2$, pH 6.1), followed by a second fixation step for 15 minutes in
704 cytoskeleton buffer (pH 7.0) containing 2% glutaraldehyde. The coverslips were incubated
705 for additional 4-12 h in cytoskeleton buffer containing 2% glutaraldehyde at 4°C, and were
706 then stained for electron microscopy. Negative staining was performed in mixtures of 4-6%
707 sodium silicotungstate (Agar Scientific) at pH 7.0, containing 10 nm gold colloid saturated
708 with BSA, and diluted 1:10 from a gold stock (Urban et al., 2010). Double tilt series of
709 negatively stained cytoskeletons were acquired on a FEI Tecnai G20 transmission electron
710 microscope (Tecnai, Hillsboro, OR) operated at 200 kV driven by SerialEM 3.x
711 (Mastronarde, 2005) equipped with an Eagle 4k HS CCD camera (Gatan, Pleasanton, CA).
712 Double axis tilt series were acquired with typical tilt angles from -65° to +65° and 1°
713 increments following the Saxton scheme at a primary on-screen magnification of 25,000x.
714 Actin filaments were tracked automatically using a Matlab-based tracking algorithm (Mueller
715 et al., 2017; Winkler et al., 2012).

716

717 **Focal adhesion analysis**

718 Focal adhesions in MV^{D7} and derived cells were analyzed from confocal images captured at
719 identical settings. Images of cells labelled for vinculin were first processed in ImageJ by
720 background subtraction using a rolling ball radius of 40 pixels, exclusion of nuclear regions

721 due to high background staining, and by contouring of cell perimeters. Preprocessed images
722 were then analyzed by the Focal Adhesion Analysis Server (Berginski and Gomez, 2013).
723 The parameters were set to imaging frequency 0 min, detection threshold 3.5 and minimal
724 adhesion size of 10 pixels. Obtained values for FA intensity and size as well as number of
725 FAs/cell were subsequently analyzed in Excel.
726
727 **Traction force analysis**
728 Patterned polyacrylamide hydrogels were fabricated according to the Mask method (Vignaud
729 et al., 2014). A quartz photomask was first cleaned through oxygen plasma (AST product,
730 300W) for 3.5 min at 200 W. Areas containing crossbow patterns were then incubated with
731 0.1 mg/mL Poly(L-lysine)-graft-poly(ethylene glycol) (PLL-g-PEG) (JenKem Technology,
732 Plano, TX) in 10mM HEPES, pH 7.4 for 30 min. After a rapid de-wetting step, PLL-PEG
733 was burned using deep-UV exposure for 6 min. Patterns on the mask were then incubated
734 with a mix of 10 µg/mL fibronectin (Sigma) and 10 µg/mL fibrinogen Alexa Fluor 647
735 conjugate (Invitrogen) in 100 mM sodium bicarbonate buffer pH, 8.4 for 30 min. A mix of
736 8% acrylamide (Sigma) and 0.264% bis-acrylamide solution (Sigma) was degassed for 30
737 min, mixed with 0.2 µm diameter PLL-PEG-coated fluorescent beads (Fluorosphere #F8810,
738 Life Technologies (Carlsbad, CA)) and sonicated before addition of APS and TEMED. 25 µL
739 of this solution was added onto the micropatterned photomask, covered with a silanized
740 coverslip, and allowed to polymerize for 25 min before being gently detached in sodium
741 bicarbonate buffer. Micropatterns were stored overnight in sodium bicarbonate buffer at 4°C
742 before plating cells. Non-patterned hydrogels were prepared using the same polyacrylamide
743 polymerization procedure followed by a step of oxygen plasma treatment for 30 sec at 30 W
744 of the coverslips and subsequent incubation with fibronectin for 30 min.

For identification of untransfected MVE-KO cells on patterns, the cells were stained with 1 µM CellTracker Green (Invitrogen) for 5 min followed by removal of unbound dye with PBS. In case of reconstituted MVE-KO cells, only cells expressing EGFP-Evl that exhibited appropriate localization of the fusion protein at focal adhesions on the patterns were selected for performing traction force experiments. Images were acquired on an EclipseTi-E Nikon confocal spinning disk microscope equipped with a CSUX1-A1 Yokogawa confocal head.

Data were analyzed with a set of macros in Fiji (Martiel et al., 2015). Displacement fields were obtained from bead images prior and after removal of cells by trypsin treatment. Bead images were first paired and aligned to correct for experimental drift. Displacement field was calculated by particle imaging velocimetry (PIV) on the base of normalized cross-correlation following an iterative scheme. Erroneous vectors where discarded owing to their low correlation value and replaced by the median value of neighboring vectors. Traction-force field was subsequently reconstructed by Fourier Transform Traction Cytometry, with a regularization parameter set to 3.2×10^{-10}.

Statistical analyses

Quantitative experiments were performed at least in triplicates to avoid any potential bias of environmental influences or unintentional error. Impact on lamellipodial or adhesion phenotypes derived from analyses on fixed samples and living cells were systematically obtained from sample sizes of dozens or hundreds of cells, respectively. Raw data were processed in Excel (Microsoft). Statistical analyses were performed using SigmaPlot 11.0 software (Systat Software, Erkrath, Germany) or GraphPad Prism 5 (GraphPad, San Diego, CA). All data sets were tested for normality by the Shapiro-Wilk test. Statistical differences between not normally distributed datasets of two groups were determined by the non-parametric Mann-Whitney U rank sum test. For comparison of more than 2 groups, statistical

770 significance of normally-distributed data was examined by one-way ANOVA and Tukey
771 Multiple Comparison test. In case of not normally-distributed data, the non-parametric
772 Kruskal-Wallis test and Dunn's Multiple Comparison test were used. Statistical differences
773 were defined as *$p \leq 0.05$, **$p \leq 0.01$, ***$p \leq 0.001$ as well as n.s., not significant, and are
774 displayed and mentioned in figures and figure legends, respectively. Graphs were created
775 with Origin 2018G (OriginLab, Northampton, Ma), and final figures prepared with
776 Photoshop (Adobe, San Jose, CA) and CorelDraw Graphics Suite 6X (CorelDraw, Ottawa,
777 On).

778

779 **Acknowledgements**

780 This work was supported in part by the Deutsche Forschungsgemeinschaft (DFG), grants
781 FA330/11-1 (to J.F.), RO2414/5-1 PROCOMPAS graduate program GRK2223/1 (to K.R.) as
782 well as by ERC Advanced grants AAA 741773 (to L.B.) and CoG 724373 (to M.S.), and the
783 Austrian Science Foundation (FWF) (to M.S.). We also thank Prof. Dr. em. Brigitte Jockusch
784 and Sabine Buchmeier (PROCOMPAS monoclonal antibody facility, TU Braunschweig) for
785 antibody generation, and the ANR-17-EURE-003 for sponsoring the live microscopy
786 facilities of DBSCI department of IRIG (MuLife).

787

788 **Competing interests:** The authors declare that no competing interests exist.

789

790 **References:**

791 Adams JC, Schwartz MA. 2000. Stimulation of fascin spikes by thrombospondin-1 is
792 mediated by the GTPases Rac and Cdc42. *J Cell Biol* **150**:807–22.
793 doi:10.1083/jcb.150.4.807
794 Aspenström P, Fransson A, Saras J. 2004. Rho GTPases have diverse effects on the

795 organization of the actin filament system. *Biochem J* **377**:327–37.
796 doi:10.1042/BJ20031041
797 Auerbuch V, Loureiro JJ, Gertler FB, Theriot JA, Portnoy DA. 2003. Ena/VASP proteins
798 contribute to Listeria monocytogenes pathogenesis by controlling temporal and spatial
799 persistence of bacterial actin-based motility. *Mol Microbiol* **49**:1361–75.
800 Bear JE, Gertler FB. 2009. Ena/VASP: towards resolving a pointed controversy at the barbed
801 end. *J Cell Sci* **122**:1947–1953. doi:10.1242/jcs.038125
802 Bear JE, Loureiro JJ, Libova I, Fässler R, Wehland J, Gertler FB. 2000. Negative regulation
803 of fibroblast motility by Ena/VASP proteins. *Cell* **101**:717–28.
804 Bear JE, Svitkina TM, Krause M, Schafer DA, Loureiro JJ, Strasser GA, Maly I V, Chaga
805 OY, Cooper JA, Borisy GG, Gertler FB. 2002. Antagonism between Ena/VASP proteins
806 and actin filament capping regulates fibroblast motility. *Cell* **109**:509–21.
807 Berg JS, Cheney RE. 2002. Myosin-X is an unconventional myosin that undergoes
808 intrafilopodial motility. *Nat Cell Biol* **4**:246–250. doi:10.1038/ncb762
809 Berginski ME, Gomez SM. 2013. The Focal Adhesion Analysis Server: a web tool for
810 analyzing focal adhesion dynamics. *F1000Research* **2**:68.
811 doi:10.12688/f1000research.2-68.v1
812 Bieling P, Hansen SD, Akin O, Li T, Hayden CC, Fletcher DA, Mullins RD. 2018. WH2 and
813 proline-rich domains of WASP-family proteins collaborate to accelerate actin filament
814 elongation. *EMBO J* **37**:102–121. doi:10.15252/embj.201797039
815 Blanchoin L, Boujemaa-Paterski R, Sykes C, Plastino J. 2014. Actin dynamics, architecture,
816 and mechanics in cell motility. *Physiol Rev* **94**:235–63. doi:10.1152/physrev.00018.2013
817 Block J, Breitsprecher D, Kühn S, Winterhoff M, Kage F, Geffers R, Duwe P, Rohn JL,
818 Baum B, Brakebusch C, Geyer M, Stradal TE, Faix J, Rottner K. 2012. FMNL2 drives
819 actin-based protrusion and migration downstream of Cdc42. *Curr Biol* **22**:1005–12.

820 doi:10.1016/j.cub.2012.03.064

821 Block J, Stradal TE, Hänisch J, Geffers R, Köstler SA, Urban E, Small JV, Rottner K, Faix J.
822 2008. Filopodia formation induced by active mDia2/Drf3. *J Microsc* **231**.
823 doi:10.1111/j.1365-2818.2008.02063.x

824 Bohil AB, Robertson BW, Cheney RE. 2006. Myosin-X is a molecular motor that functions
825 in filopodia formation. *Proc Natl Acad Sci* **103**:12411–12416.
826 doi:10.1073/pnas.0602443103

827 Breitsprecher D, Kiesewetter AK, Linkner J, Urbanke C, Resch GP, Small JV, Faix J. 2008.
828 Clustering of VASP actively drives processive, WH2 domain-mediated actin filament
829 elongation. *EMBO J* **27**:2943–2954. doi:10.1038/emboj.2008.211

830 Breitsprecher D, Kiesewetter AK, Linkner J, Vinzenz M, Stradal TEB, Small JV, Curth U,
831 Dickinson RB, Faix J. 2011a. Molecular mechanism of Ena/VASP-mediated actin-
832 filament elongation. *EMBO J* **30**:456–467. doi:10.1038/emboj.2010.348

833 Breitsprecher D, Koestler SA, Chizhov I, Nemethova M, Mueller J, Goode BL, Small JV,
834 Rottner K, Faix J. 2011b. Cofilin cooperates with fascin to disassemble filopodial actin
835 filaments. *J Cell Sci* **124**:3305–3318. doi:10.1242/jcs.086934

836 Brinkman EK, Chen T, Amendola M, van Steensel B. 2014. Easy quantitative assessment of
837 genome editing by sequence trace decomposition. *Nucleic Acids Res* **42**:e168.
838 doi:10.1093/nar/gku936

839 Brühmann S, Ushakov DS, Winterhoff M, Dickinson RB, Curth U, Faix J. 2017. Distinct
840 VASP tetramers synergize in the processive elongation of individual actin filaments
841 from clustered arrays. *Proc Natl Acad Sci* **114**:E5815–E5824.
842 doi:10.1073/pnas.1703145114

843 Dimchev G, Rottner K. 2018. Micromanipulation Techniques Allowing Analysis of
844 Morphogenetic Dynamics and Turnover of Cytoskeletal Regulators. *J Vis Exp*.

doi:10.3791/57643

Eden S, Rohatgi R, Podtelejnikov A V., Mann M, Kirschner MW. 2002. Mechanism of regulation of WAVE1-induced actin nucleation by Rac1 and Nck. *Nature* **418**:790–793. doi:10.1038/nature00859

Faix J, Breitsprecher D, Stradal TE, Rottner K. 2009. Filopodia: Complex models for simple rods. *Int J Biochem Cell Biol* **41**. doi:10.1016/j.biocel.2009.02.012

Faix J, Weber I, Mintert U, Köhler J, Lottspeich F, Marriott G. 2001. Recruitment of cortexillin into the cleavage furrow is controlled by Rac1 and IQGAP-related proteins. *EMBO J* **20**:3705–15. doi:10.1093/emboj/20.14.3705

Fradelizi J, Noireaux V, Plastino J, Menichi B, Louvard D, Sykes C, Golsteyn RM, Friederich E. 2001. ActA and human zyxin harbour Arp2/3-independent actin-polymerization activity. *Nat Cell Biol* **3**:699–707. doi:10.1038/35087009

Galler AB, García Arguinzonis MI, Baumgartner W, Kuhn M, Smolenski A, Simm A, Reinhard M. 2006. VASP-dependent regulation of actin cytoskeleton rigidity, cell adhesion, and detachment. *Histochem Cell Biol* **125**:457–474. doi:10.1007/s00418-005-0091-z

Gateva G, Tojkander S, Koho S, Carpen O, Lappalainen P. 2014. Palladin promotes assembly of non-contractile dorsal stress fibers through VASP recruitment. *J Cell Sci* **127**:1887–1898. doi:10.1242/jcs.135780

Geese M, Loureiro JJ, Bear JE, Wehland J, Gertler FB, Sechi AS. 2002. Contribution of Ena/VASP proteins to intracellular motility of listeria requires phosphorylation and proline-rich core but not F-actin binding or multimerization. *Mol Biol Cell* **13**:2383–96. doi:10.1091/mbc.e02-01-0058

Gertler FB, Niebuhr K, Reinhard M, Wehland J, Soriano P. 1996. Mena, a relative of VASP and Drosophila Enabled, is implicated in the control of microfilament dynamics. *Cell*

87:227–39.

Gupton SL, Anderson KL, Kole TP, Fischer RS, Ponti A, Hitchcock-DeGregori SE, Danuser G, Fowler VM, Wirtz D, Hanein D, Waterman-Storer CM. 2005. Cell migration without a lamellipodium: translation of actin dynamics into cell movement mediated by tropomyosin. *J Cell Biol* **168**:619. doi:10.1083/JCB.200406063

Gupton SL, Riquelme D, Hughes-Alford SK, Tadros J, Rudina SS, Hynes RO, Lauffenburger D, Gertler FB. 2012. Mena binds α5 integrin directly and modulates α5β1 function. *J Cell Biol* **198**:657–76. doi:10.1083/jcb.201202079

Han Y-H, Chung CY, Wessels D, Stephens S, Titus MA, Soll DR, Firtel RA. 2002. Requirement of a Vasodilator-stimulated Phosphoprotein Family Member for Cell Adhesion, the Formation of Filopodia, and Chemotaxis in Dictyostelium. *J Biol Chem* **277**:49877–49887. doi:10.1074/jbc.M209107200

Hansen SD, Mullins RD. 2015. Lamellipodin promotes actin assembly by clustering Ena/VASP proteins and tethering them to actin filaments. *Elife* **4**:1–29. doi:10.7554/eLife.06585

Hansen SD, Mullins RD. 2010. VASP is a processive actin polymerase that requires monomeric actin for barbed end association. *J Cell Biol* **191**:571–584. doi:10.1083/jcb.201003014

Harris ES, Gauvin TJ, Heimsath EG, Higgs HN. 2010. Assembly of filopodia by the formin FRL2 (FMNL3). *Cytoskeleton* **67**:755–772. doi:10.1002/cm.20485

Innocenti M, Zucconi A, Disanza A, Frittoli E, Areces LB, Steffen A, Stradal TE, Fiore PP Di, Carlier M-F, Scita G. 2004. Abi1 is essential for the formation and activation of a WAVE2 signalling complex. *Nat Cell Biol* **6**:319–327. doi:10.1038/ncb1105

Ismail AM, Padrick SB, Chen B, Umetani J, Rosen MK. 2009. The WAVE regulatory complex is inhibited. *Nat Struct Mol Biol* **16**:561–3. doi:10.1038/nsmb.1587

895 Kage F, Winterhoff M, Dimchev V, Mueller J, Thalheim T, Freise A, Brühmann S, Kollasser
896 J, Block J, Dimchev G, Geyer M, Schnittler H-J, Brakebusch C, Stradal TE, Carlier M-
897 F, Sixt M, Käs J, Faix J, Rottner K. 2017. FMNL formins boost lamellipodial force
898 generation. *Nat Commun* **8**. doi:10.1038/ncomms14832
899 Kanchanawong P, Shtengel G, Pasapera AM, Ramko EB, Davidson MW, Hess HF,
900 Waterman-Storer CM. 2010. Nanoscale architecture of integrin-based cell adhesions.
901 *Nature* **468**:580–584. doi:10.1038/nature09621
902 Kang N, Yaqoob U, Geng Z, Bloch K, Liu C, Gomez T, Billadeau D, Shah V. 2010. Focal
903 Adhesion Assembly in Myofibroblasts Fosters a Microenvironment that Promotes
904 Tumor Growth. *Am J Pathol* **177**:1888–1900. doi:10.2353/ajpath.2010.100187
905 Koestler SA, Auinger S, Vinzenz M, Rottner K, Small JV. 2008. Differentially oriented
906 populations of actin filaments generated in lamellipodia collaborate in pushing and
907 pausing at the cell front. *Nat Cell Biol* **10**:306–13. doi:10.1038/ncb1692
908 Koestler SA, Steffen A, Nemethova M, Winterhoff M, Luo N, Holleboom JM, Krupp J,
909 Jacob S, Vinzenz M, Schur F, Schlüter K, Gunning PW, Winkler C, Schmeiser C, Faix
910 J, Stradal TE, Small JV, Rottner K. 2013. Arp2/3 complex is essential for actin network
911 treadmilling as well as for targeting of capping protein and cofilin. *Mol Biol Cell*
912 **24**:2861–75. doi:10.1091/mbc.E12-12-0857
913 Kovar DR, Harris ES, Mahaffy R, Higgs HN, Pollard TD. 2006. Control of the Assembly of
914 ATP- and ADP-Actin by Formins and Profilin. *Cell* **124**:423–435.
915 doi:10.1016/j.cell.2005.11.038
916 Kwiatkowski A V., Rubinson DA, Dent EW, Edward van Veen J, Leslie JD, Zhang J,
917 Mebane LM, Philippar U, Pinheiro EM, Burds AA, Bronson RT, Mori S, Fässler R,
918 Gertler FB. 2007. Ena/VASP Is Required for neuritogenesis in the developing cortex.
919 *Neuron* **56**:441–55. doi:10.1016/j.neuron.2007.09.008

920 Lai FPL, Szczodrak M, Block J, Faix J, Breitsprecher D, Mannherz HG, Stradal TE, Dunn
921 GA, Small JV, Rottner K. 2008. Arp2/3 complex interactions and actin network turnover
922 in lamellipodia. *EMBO J* **27**:982–92. doi:10.1038/emboj.2008.34
923 Lai FPL, Szczodrak M, Oelkers JM, Ladwein M, Acconcia F, Benesch S, Auinger S, Faix J,
924 Small JV, Polo S, Stradal TE, Rottner K. 2009. Cortactin promotes migration and
925 platelet-derived growth factor-induced actin reorganization by signaling to Rho-
926 GTPases. *Mol Biol Cell* **20**. doi:10.1091/mbc.E08-12-1180
927 Letort G, Ennomani H, Gressin L, Théry M, Blanchoin L. 2015. Dynamic reorganization of
928 the actin cytoskeleton. *F1000Research* **4**:940. doi:10.12688/f1000research.6374.1
929 Litschko C, Damiano-Guercio J, Brühmann S, Faix J. 2018. Analysis of Random Migration
930 of Dictyostelium Amoeba in Confined and Unconfined EnvironmentsMethods in
931 Molecular Biology (Clifton, N.J.). pp. 341–350. doi:10.1007/978-1-4939-7701-7_24
932 Loisel TP, Boujemaa R, Pantaloni D, Carlier M-F. 1999. Reconstitution of actin-based
933 motility of Listeria and Shigella using pure proteins. *Nature* **401**:613–616.
934 doi:10.1038/44183
935 Martiel J-L, Leal A, Kurzawa L, Balland M, Wang I, Vignaud T, Tseng Q, Théry M. 2015.
936 Measurement of cell traction forces with ImageJ. *Methods Cell Biol* **125**:269–87.
937 doi:10.1016/bs.mcb.2014.10.008
938 Mastronarde DN. 2005. Automated electron microscope tomography using robust prediction
939 of specimen movements. *J Struct Biol* **152**:36–51. doi:10.1016/j.jsb.2005.07.007
940 Mellor H. 2010. The role of formins in filopodia formation. *Biochim Biophys Acta* **1803**:191–
941 200. doi:10.1016/j.bbamcr.2008.12.018
942 Molinie N, Gautreau A. 2018. The Arp2/3 Regulatory System and Its Deregulation in Cancer.
943 *Physiol Rev* **98**:215–238. doi:10.1152/physrev.00006.2017
944 Mueller J, Szep G, Nemethova M, de Vries I, Lieber AD, Winkler C, Kruse K, Small JV,

945 Schmeiser C, Keren K, Hauschild R, Sixt M. 2017. Load Adaptation of Lamellipodial
946 Actin Networks. *Cell* **171**:188-200.e16. doi:10.1016/j.cell.2017.07.051
947 Mullins RD, Heuser JA, Pollard TD. 1998. The interaction of Arp2/3 complex with actin:
948 nucleation, high affinity pointed end capping, and formation of branching networks of
949 filaments. *Proc Natl Acad Sci U S A* **95**:6181–6. doi:10.1073/pnas.95.11.6181
950 Narita A, Mueller J, Urban E, Vinzenz M, Small JV, Maéda Y. 2012. Direct Determination of
951 Actin Polarity in the Cell. *J Mol Biol* **419**:359–368. doi:10.1016/j.jmb.2012.03.015
952 Nemethova M, Auinger S, Small JV. 2008. Building the actin cytoskeleton: filopodia
953 contribute to the construction of contractile bundles in the lamella. *J Cell Biol*
954 **180**:1233–1244. doi:10.1083/jcb.200709134
955 Olazabal IM, Caron E, May RC, Schilling K, Knecht DA, Machesky LM. 2002. Rho-kinase
956 and myosin-II control phagocytic cup formation during CR, but not FcgammaR,
957 phagocytosis. *Curr Biol* **12**:1413–18.
958 Oldenbourg R, Katoh K, Danuser G. 2000. Mechanism of Lateral Movement of Filopodia
959 and Radial Actin Bundles across Neuronal Growth Cones. *Biophys J* **78**:1176–1182.
960 doi:10.1016/S0006-3495(00)76675-6
961 Pellegrin S, Mellor H. 2005. The Rho Family GTPase Rif Induces Filopodia through mDia2.
962 *Curr Biol* **15**:129–133. doi:10.1016/j.cub.2005.01.011
963 Pollard TD. 2007. Regulation of Actin Filament Assembly by Arp2/3 Complex and Formins.
964 *Annu Rev Biophys Biomol Struct* **36**:451–477.
965 doi:10.1146/annurev.biophys.35.040405.101936
966 Pollard TD, Borisy GG. 2003. Cellular motility driven by assembly and disassembly of actin
967 filaments. *Cell* **112**:453–65.
968 Puleo JI, Parker SS, Roman MR, Watson AW, Eliato KR, Peng L, Saboda K, Roe DJ, Ros R,
969 Gertler FB, Mouneimne G. 2019. Mechanosensing during directed cell migration

970 requires dynamic actin polymerization at focal adhesions. *J Cell Biol*
971 **218**:jcb.201902101. doi:10.1083/jcb.201902101
972 Ran FA, Hsu PD, Wright J, Agarwala V, Scott DA, Zhang F. 2013. Genome engineering
973 using the CRISPR-Cas9 system. *Nat Protoc* **8**:2281–2308. doi:10.1038/nprot.2013.143
974 Reinhard M, Giehl K, Abel K, Haffner C, Jarchau T, Hoppe V, Jockusch BM, Walter U.
975 1995. The proline-rich focal adhesion and microfilament protein VASP is a ligand for
976 profilins. *EMBO J* **14**:1583–9.
977 Richter KN, Revelo NH, Seitz KJ, Helm MS, Sarkar D, Saleeb RS, D'Este E, Eberle J,
978 Wagner E, Vogl C, Lazaro DF, Richter F, Coy-Vergara J, Coceano G, Boyden ES,
979 Duncan RR, Hell SW, Lauterbach MA, Lehnart SE, Moser T, Outeiro TF, Rehling P,
980 Schwappach B, Testa I, Zapiec B, Rizzoli SO. 2018. Glyoxal as an alternative fixative to
981 formaldehyde in immunostaining and super-resolution microscopy. *EMBO J* **37**:139–
982 159. doi:10.15252/embj.201695709
983 Riedl J, Crevenna AH, Kessenbrock K, Yu JH, Neukirchen D, Bista M, Bradke F, Jenne D,
984 Holak TA, Werb Z, Sixt M, Wedlich-Soldner R. 2008. Lifeact: a versatile marker to
985 visualize F-actin. *Nat Methods* **5**:605–607. doi:10.1038/nmeth.1220
986 Rottner K, Behrendt B, Small J V, Wehland J. 1999. VASP dynamics during lamellipodia
987 protrusion. *Nat Cell Biol* **1**:321–2. doi:10.1038/13040
988 Rottner K, Faix J, Bogdan S, Linder S, Kerkhoff E. 2017. Actin assembly mechanisms at a
989 glance. *J Cell Sci* **130**. doi:10.1242/jcs.206433
990 Rottner K, Krause M, Gimona M, Small JV, Wehland J. 2001. Zyxin Is not Colocalized with
991 Vasodilator-stimulated Phosphoprotein (VASP) at Lamellipodial Tips and Exhibits
992 Different Dynamics to Vinculin, Paxillin, and VASP in Focal Adhesions. *Mol Biol Cell*
993 **12**:3103–3113. doi:10.1091/mbc.12.10.3103
994 Samarin S, Romero S, Kocks C, Didry D, Pantaloni D, Carlier M-F. 2003. How VASP

995 enhances actin-based motility. *J Cell Biol* **163**:131–142. doi:10.1083/jcb.200303191
996 Schaks M, Singh SP, Kage F, Thomason P, Klünemann T, Steffen A, Blankenfeldt W,
997 Stradal TE, Insall RH, Rottner K. 2018. Distinct Interaction Sites of Rac GTPase with
998 WAVE Regulatory Complex Have Non-redundant Functions in Vivo. *Curr Biol*
999 **28**:3674-3684.e6. doi:10.1016/j.cub.2018.10.002
1000 Scott JA, Shewan AM, den Elzen NR, Loureiro JJ, Gertler FB, Yap AS. 2006. Ena/VASP
1001 Proteins Can Regulate Distinct Modes of Actin Organization at Cadherin-adhesive
1002 Contacts. *Mol Biol Cell* **17**:1085–1095. doi:10.1091/mbc.e05-07-0644
1003 Skoble J, Auerbuch V, Goley ED, Welch MD, Portnoy DA. 2001. Pivotal role of VASP in
1004 Arp2/3 complex–mediated actin nucleation, actin branch-formation, and *Listeria*
1005 *monocytogenes* motility. *J Cell Biol* **155**:89–100. doi:10.1083/jcb.200106061
1006 Small J V. 1988. The actin cytoskeleton. *Electron Microsc Rev* **1**:155–74.
1007 Steffen A, Faix J, Resch GP, Linkner J, Wehland J, Small JV, Rottner K, Stradal TE. 2006.
1008 Filopodia formation in the absence of functional WAVE- and Arp2/3-complexes. *Mol*
1009 *Biol Cell* **17**. doi:10.1091/mbc.E05-11-1088
1010 Steffen A, Ladwein M, Dimchev GA, Hein A, Schwenkmezger L, Arens S, Ladwein KI,
1011 Holleboom JM, Schur F, Small JV, Schwarz J, Gerhard R, Faix J, Stradal TE,
1012 Brakebusch C, Rottner K. 2013. Rac function is crucial for cell migration but is not
1013 required for spreading and focal adhesion formation. *J Cell Sci* **126**:4572–4588.
1014 doi:10.1242/jcs.118232
1015 Steffen A, Rottner K, Ehinger J, Innocenti M, Scita G, Wehland J, Stradal TE. 2004. Sra-1
1016 and Nap1 link Rac to actin assembly driving lamellipodia formation. *EMBO J* **23**:749–
1017 59. doi:10.1038/sj.emboj.7600084
1018 Suraneni P, Rubinstein B, Unruh JR, Durnin M, Hanein D, Li R. 2012. The Arp2/3 complex
1019 is required for lamellipodia extension and directional fibroblast cell migration. *J Cell*

Biol **197**:239–251. doi:10.1083/jcb.201112113

Svitkina TM, Bulanova EA, Chaga OY, Vignjevic DM, Kojima S, Vasiliev JM, Borisy GG. 2003. Mechanism of filopodia initiation by reorganization of a dendritic network. *J Cell Biol* **160**:409–421. doi:10.1083/jcb.200210174

Urban E, Jacob S, Nemethova M, Resch GP, Small JV. 2010. Electron tomography reveals unbranched networks of actin filaments in lamellipodia. *Nat Cell Biol* **12**:429–435. doi:10.1038/ncb2044

Vignaud T, Ennomani H, Théry M. 2014. Polyacrylamide Hydrogel MicropatterningMethods in Cell Biology. pp. 93–116. doi:10.1016/B978-0-12-417136-7.00006-9

Vignjevic DM, Kojima S, Aratyn Y, Danciu O, Svitkina TM, Borisy GG. 2006. Role of fascin in filopodial protrusion. *J Cell Biol* **174**:863–875. doi:10.1083/jcb.200603013

Vinzenz M, Nemethova M, Schur F, Mueller J, Narita A, Urban E, Winkler C, Schmeiser C, Koestler SA, Rottner K, Resch GP, Maeda Y, Small J V. 2012. Actin branching in the initiation and maintenance of lamellipodia. *J Cell Sci* **125**:2775–2785. doi:10.1242/jcs.107623

Winkler C, Vinzenz M, Small JV, Schmeiser C. 2012. Actin filament tracking in electron tomograms of negatively stained lamellipodia using the localized radon transform. *J Struct Biol* **178**:19–28. doi:10.1016/j.jsb.2012.02.011

Wu C, Asokan SB, Berginski ME, Haynes EM, Sharpless NE, Griffith JD, Gomez SM, Bear JE. 2012. Arp2/3 Is Critical for Lamellipodia and Response to Extracellular Matrix Cues but Is Dispensable for Chemotaxis. *Cell* **148**:973–987. doi:10.1016/j.cell.2011.12.034

Yang C, Czech L, Gerboth S, Kojima S, Scita G, Svitkina T. 2007. Novel Roles of Formin mDia2 in Lamellipodia and Filopodia Formation in Motile Cells. *PLoS Biol* **5**:e317. doi:10.1371/journal.pbio.0050317

Young LE, Heimsath EG, Higgs HN. 2015. Cell type-dependent mechanisms for formin-

mediated assembly of filopodia. *Mol Biol Cell* **26**:4646–4659. doi:10.1091/mbc.E15-09-0626

Young LE, Higgs HN. 2018. Focal Adhesions Undergo Longitudinal Splitting into Fixed-Width Units. *Curr Biol* **28**:2033-2045.e5. doi:10.1016/j.cub.2018.04.073

Young LE, Latario CJ, Higgs HN. 2018. Roles for Ena/VASP proteins in FMNL3-mediated filopodial assembly. *J Cell Sci* **131**:jcs220814. doi:10.1242/jcs.220814

Figures

Figure 1. Loss of Ena/VASP-proteins impairs cell migration in B16-F1 cells. (**A**) To obtain independent triple-knockout mutant cell lines, the two independent Evl single knockout mutants (E-KO #23 and #27) derived from B16-F1 mouse melanoma cells, were separately used to the generate independent Evl/VASP double mutants (E/V-KO #23.7 and #27.9) followed by generation of two individual triple-KO mutants additionally lacking Mena (E/V/M-KO #23.7.66 and #27.9.12). Elimination of Evl, VASP and all Mena isoforms by CRISPR/Cas9 in B16-F1 cells was confirmed by immunoblotting using specific antibodies (asterisk indicates nonspecific band). GAPDH was used as loading control. (**B**) Consecutive gene disruption of the three Ena/VASP paralogues increasingly diminishes cell migration on laminin. At least three time-lapse movies from three independent experiments were analyzed for each cell line. (**C**) Directionality increased with consecutive inactivation of the three Ena/VASP paralogues. Bars represent arithmetic means ± SD. (**D**) Distribution of turning angles during migration of B16-F1 and derived mutant cells. (**E-G**) Cell speed and directionality are largely rescued by ectopic expression of EGFP-tagged VASP, Evl or Mena in EVM-KO #23 cells. (**F**) Bars represent arithmetic means ± SD. (**G**) Analyses of mean square displacement of wild-type *versus* mutant cells. Respective symbols and error bars represent means ± SEM. (B-E) The boxes in box plots indicate 50% (25-75%) and whiskers

(5-95%) of all measurements, with dashed black lines depicting the medians, arithmetic means are highlighted in red. (B-C) and (E-F) Non-parametric, Kruskal-Wallis test and Dunn's Multiple Comparison test were used to reveal statistically significant differences between datasets. *p <0.05, **p <0.01, ***p <0.001; n.s.; not significant. n, number of cells analyzed from at least 3 independent experiments.

The following video and figure supplement are available for figure 1:

Figure 1-figure supplement 1. Loss of Ena/VASP proteins affects migration and directionality. (**A**) Distribution of turning angles during migration of EVM-KO cells reconstituted with VASP, Evl or Mena. As opposed to Mena, VASP and Evl both readily rescued turning angles. (**B)** Analyses of mean square displacement of mutant and reconstituted cells. All three Ena/VASP members rescued migration as assessed by MSD, but VASP was most efficient. Respective symbols and error bars represent means ± SEM.

Figure 1-video 1. Loss of Ena/VASP proteins in B16-F1 cells impairs cell migration, related to ***Figure 1***. Random migration of B16-F1, and derived Evl-KO (E-KO), Evl/VASP-KO (EV-KO) and Evl/VASP/Mena-KO (EVM-KO) mutants on laminin. Cells were recorded by phase-contrast time-lapse imaging using a 4x objective and tracked by MTrackJ to illustrate representative cell trajectories. Note more directional movement of EVM-KO cells. Time is indicated in h:min. Bar, 300 µm.

Figure 2. Inactivation of Ena/VASP proteins in various fibroblasts impairs cell migration. (**A**) MV^{D7} cells lack Mena and VASP, but still express Evl. Elimination of Evl by CRISPR/Cas9 in MV^{D7} fibroblasts was confirmed by immunoblotting in independent clonal cell lines (MVE-KO). GAPDH was used as loading control. Asterisk indicates nonspecific

band in Mena blot. (**B**) Elimination of Evl in MV^{D7} cells decreased cell speed on fibronectin-coated glass and could be rescued by expression of Evl. (**C**) Analyses of mean square displacement of MV^{D7}, MVE-KO and reconstituted cells as indicated. Data points represent arithmetic means ± SEM. At least three time-lapse movies from three independent experiments were analyzed for each cell line. (**D**) Representative frames from wound healing movies of MV^{D7}, MVE-KO and reconstituted cells as indicated. MVE-KO cells were not able to close the wound after 17 hours. Bar, 200 µm. (**E**) Reduction of wound area over time. n, number of movies analyzed. Data are means ± SD. (**F**) Average wound closure rate. n, number of movies analyzed. (**G**) Immunoblot of independent single and double-KO mutants derived from NIH 3T3 fibroblasts lacking Mena (M-KO) or Mena and VASP (MV-KO) by CRISPR/Cas9 technology. GAPDH was used as loading control. (**H**) Consistent with findings in B16-F1 cells, consecutive gene disruption of these two Ena/VASP paralogues in NIH 3T3 fibroblasts again increasingly diminished cell migration on fibronectin. (**I**) Analyses of mean square displacement of NIH 3T3, M-KO and MV-KO cells as indicated. Data points represent arithmetic means ± SEM. n, number of cells tracked. At least three time-lapse movies from three independent experiments were analyzed for each cell line. (**J**) Total cytoplasmic concentrations of Ena/VASP proteins in investigated cell lines. (B, F and H) Boxes in box plots indicate 50% (25-75%) and whiskers (5-95%) of all measurements, with dashed black lines depicting the medians, arithmetic means are highlighted in red. Non-parametric, Kruskal-Wallis test and Dunn's Multiple Comparison test were used to reveal statistically significant differences between datasets. *p <0.05, **p <0.01, ***p <0.001; n.s.; not significant. n, number of cells analyzed from at least 3 independent experiments.

The following figure supplement is available for figure 2:

Figure 2-figure supplement 1. Elimination of Evl in MV^{D7} cells affects directionality. (**A**) Quantification of directionality. Bars represent arithmetic means ± SD. ***p<0.001 and n.s., not significant by Kruskal-Wallis test and Dunn's Multiple Comparison test and n, number of cells analyzed. **(B)** Radar plots showing trajectories of 15 randomly migrating MV^{D7}, MVE-KO and reconstituted cells as indicated. Note higher directional persistence of MVE-KO cells compared to MV^{D7} cells, which was diminished again by expression of Evl. Scale bar, 100 µm.

Figure 3. Loss of Ena/VASP perturbs lamellipodia and abrogates microspike formation in B16-F1 cells. (**A**) Representative examples of lamellipodia from wild-type B16-F1, EVM-KO and reconstituted EVM-KO cells transiently expressing EGFP-VASP. Cells migrating on laminin and stained for the actin cytoskeleton with phalloidin. Bar, 10 µm. (**B**) Quantification of F-actin intensities in lamellipodia (red circle in A) of wild-type and mutant cells after subtraction of background (blue circle in A). (**C**) Quantification of lamellipodia width in wild-type and mutant cells. (**D**) Loss of Ena/VASP markedly diminishes fascin-decorated microspikes, which are rescued by EGFP-VASP. Immunostaining with fascin antibody. Bar, 10 µm. (**E**) Quantification of microspikes in wild-type and mutant cells. (**F**) Quantification of microspike length in wild-type and mutant cells. (**G**) Comparable expression of fascin in wild-type and EVM-KO cells was confirmed by immunoblotting using fascin-specific antibodies. GAPDH was used as loading control. (**H**) Representative examples of lamellipodia from wild-type B16-F1 cells, single E-KO, double EV-KO and triple EVM-KO mutants. Displayed cells migrating on laminin were fixed and stained with phalloidin to visualize their F-actin cytoskeleton. Bars, 10 µm. Note presence of microspikes in B16-F1 wild-type cells, single E-KO and double EV-KO mutants, but not in the triple EVM-KO mutant cell. (B-C and E-F) Boxes in box plots indicate 50% (25-75%) and whiskers (5-95%)

of all measurements, with dashed black lines depicting the medians, arithmetic means are highlighted in red. Non-parametric, Kruskal-Wallis test and Dunn's Multiple Comparison test were used to reveal statistically significant differences between datasets. ***p <0.001; n.s.; not significant. n, number of cells analyzed (B, C, and E) or microspikes (F) from at least 3 independent experiments.

The following video and figure supplement are available for figure 3:

Figure 3-figure supplement 1. Expression of Evl and Mena is sufficient for rescuing of lamellipodia in B16-F1 cells. **(A)** Representative examples of lamellipodia in wild-type B16-F1, EVM-KO and reconstituted EVM-KO cells transiently expressing EGFP-Evl or -Mena, as indicated. Cells migrating on laminin were fixed and stained with phalloidin to visualize the actin cytoskeleton. Bar, 10 µm. (**B**) Quantification of F-actin intensities in lamellipodia of wild-type, mutant and reconstituted cells after background subtraction. (**C**) Quantification of lamellipodia widths in cells indicated. (B-C) Boxes in box plots indicate 50% (25-75%) and whiskers (5-95%) of all measurements, with dashed black lines depicting the medians, arithmetic means are highlighted in red. Non-parametric, Kruskal-Wallis test and Dunn's Multiple Comparison test were used to reveal statistically significant differences between datasets. *p <0.05, **p <0.01, ***p <0.001; n.s.; not significant. n, number of cells analyzed from at least 3 independent experiments.

Figure 3-video 1. Elimination of all three Ena/VASP proteins impairs lamellipodium formation and abolishes microspikes, related to ***Figure 3***. Displayed cells were transfected with EGFP-LifeAct to monitor actin dynamics during migration on laminin by time-lapse imaging using a 40x objective. EVM-KO cells were additionally transfected with mCherry-

VASP (not shown). Reconstitution of EVM-KO cells with mCherry-VASP restored lamellipodium and microspike formation. Time is indicated in min:s. Bar, 15 µm.

Figure 3-video 2. Elimination of all three Ena/VASP proteins abrogates microspikes, related to ***Figure 3***. The cells shown were transfected with EGFP-fascin to monitor microspikes in cells migrating on laminin by time-lapse imaging using a 40x objective. EVM-KO cells were additionally transfected with mCherry-VASP (not shown). Reconstitution of EVM-KO cells with mCherry-VASP fully restored microspike formation (right panel). Time is indicated in min:s. Bar, 15 µm.

Figure 4. Microspike formation is exclusively rescued by all three Ena/VASP members, but not by active Rif-L77, myosin X, active mDia2ΔDAD or active FMNL2 and -3. (**A**) Images display cells stained for the actin cytoskeleton with phalloidin and respective, expressed EGFP-tagged protein as indicated. Bars, 20 µm. (**B**) EVM-KO cells form filopodia in the absence of lamellipodia. Representative examples of phalloidin-stained wild-type B16-F1 and EVM-KO cells devoid of lamellipodia after treatment with 200 µM CK666 seeded at low laminin (1µg/mL). Bar, 10 µm. (**C**) Quantification of filopodia in CK666-treated B16-F1 and EVM-KO cells. (**D**) Unchanged filopodium formation in B16-F1 and EVM-KO cells triggered by transient expression of active mDia2. Representative examples of B16-F1 and EVM-KO cells after labelling with GFP nanobodies are shown. Bar, 10 µm. (**E**) Quantification of filopodia revealed no difference between wild-type and mutant cells. (C and E) Boxes in box plots indicate 50% (25-75%) and whiskers (5-95%) of all measurements, with dashed black lines depicting the medians, arithmetic means are highlighted in red. Non-parametric, by Mann-Whitney U rank sum test was used to reveal statistically significant

differences between datasets. ***p <0.001; n.s.; not significant. n, number of cells analyzed from at least 3 independent experiments.

The following figure supplement is available for figure 4:

Figure 4-figure supplement 1. Quantification of microspikes after rescue of EVM-KO cells with EGFP-tagged Evl or Mena. **(A)** Quantification of microspikes per cell. (**B**) Quantification of microspike length. Note longer microspikes in reconstituted EVM-KO cells expressing Mena. (A-B) **p<0.01, ***p<0.001; n.s. not significant by Kruskal-Wallis test and Dunn's Multiple Comparison test. n, number of cells analyzed.

Figure 5. Loss of Ena/VASP affects lamellipodial parameters and protrusion dynamics. (**A**) Immunolabelling of the Arp2/3 complex subunit p16-ARC (ArpC5A) in wild-type, mutant and reconstituted cells as indicated. Bar, 10 µm. (**B**) Quantification of Arp2/3 complex intensities in lamellipodia. (**C**) Quantification of Arp2/3 complex signal width. (**D**) Immunolabelling of CP in cell types as indicated. Bar, 10 µm. (**E**) Quantification of CP signal intensities in lamellipodia. (**F**) Quantification of CP signal width in lamellipodia. (**G**) Loss of Ena/VASP reduces the efficiency of lamellipodium protrusion. Kymographs of representative phase-contrast movies are shown. Bar, 10 µm. (**H**) Multiple examples of lamellipodium protrusion in B16-F1 *versus* EVM-KO *versus* EVM-KO cells reconstituted with VASP. (**I**) Quantification of protrusion rates. B-C, E-F and I, *p<0.05, ***p<0.001 and n.s., not significant by Kruskal-Wallis test and Dunn's Multiple Comparison test. n, number of cells. (**J**) Quantification of protrusion persistence. (**K**) FRAP of EGFP-ß-actin in lamellipodia of B16-F1 and EVM-KO cells bleached as indicated by white rectangles. Numbers in post-bleach images correspond to seconds after bleach. Bar, 3 µm. (**L**) Average actin assembly rates of respective cell types expressing EGFP-ß-actin. Note reduced

lamellipodial actin assembly in the mutant. J-L, ***p <0.001, n.s., not significant by Mann-Whitney U rank sum test. n, number of cells analyzed.

The following video and figure supplement are available for figure 5:

Figure 5-figure supplement 1. Loss of Ena/VASP affects additional lamellipodial parameters. (**A)** Immunolabelling of endogenous Arp2/3 complex subunit p16-ARC (ArpC5A) in B16-F1 wild-type, EVM-KO and reconstituted EVM-KO cells expressing Evl or Mena. Bar, 10 µm. (**B**) Quantification of p16-ARC intensities in lamellipodia. (**C**) Quantification of p16-ARC width. (**D**) Immunolabelling of endogenous CP in wild-type, mutant and reconstituted cells. Bar, 10 µm. (**E**) Quantification of CP intensities in lamellipodia. (**F**) Quantification of CP width in lamellipodia. (**G**) Immunolabelling of endogenous cortactin in wild-type, mutant and reconstituted cells. Bar, 10 µm. (**H**) Quantification of cortactin intensities in lamellipodia. (**I**) Quantification of cortactin width in lamellipodia. B-C, E-F and H-I, * p< 0.05, **p<0.01, ***p<0.001, n.s., not significant by Kruskal-Wallis test and Dunn's Multiple Comparison test. n, number of cells analyzed. (**J-K**) Immunolabelling of endogenous WAVE2 revealed no differences between B16-F1 wild-type and EVM-KO cells. Bar, 10 µm. n.s., not significant by Mann-Whitney U rank sum test. n, number of analyzed cells. (**L**) Comparable amounts of expression of WAVE2 in wild-type and EVM-KO cells were confirmed by immunoblotting using WAVE2-specific antibodies. GAPDH was used as loading control.

Figure 5-video 1. Impaired protrusion of EVM-KO cells migrating on laminin, related to ***Figure 5***. Reconstitution of the triple mutant cells with EGFP-VASP fully restored lamellipodial protrusion. Cells were recorded by time-lapse phase-contrast imaging using a 40x objective. Time is indicated in min:s. Bar, 15 µm.

Figure 5-video 2. Loss of Ena/VASP in B16-F1 cells reduces actin network polymerization, related to ***Figure 5***. Representative time-lapse movies showing FRAP experiments on lamellipodia of B16-F1 wild-type or EVM-KO cells, as indicated, expressing EGFP-β-actin on laminin. Time-lapse movies show periods before and after bleaching of lamellipodial regions with bleaching time points set to 0 sec in each case. Bar, 3 µm.

Figure 6. Electron tomography of ultrastructural changes in lamellipodial actin networks. (**A**) Transmission electron micrographs of representative wild-type (B16-F1) and EVM-KO cells showing distinct actin filament networks at the leading edge (left), and 2D projections of digital 3D tomograms showing either actin filament trajectories in green (middle), or barbed ends on grey filaments in red, and pointed ends in blue (right). Scale bar, 100 nm. (**B**) Quantification of filament length in wild-type and EVM-KO cells. ***p <0.001 by Mann-Whitney U rank sum test. Whiskers indicate 10% and 90% confidence intervals. n indicates the number of filaments analyzed. Dashed black lines show median, red lines arithmetic mean. (**C**) Densities of filaments, barbed and pointed ends in 106 nm-wide spatial bins throughout the lamellipodium. Error bars indicate SEM. 6 tomograms for each cell line were analyzed. (**D**) Histogram showing frequencies of filament angles to the leading edge (90° corresponding to filaments perpendicular to the leading edge). Dashed black lines are medians, and red lines arithmetic means.

The following video is available for figure 6:

Figure 6-video 1. Loss of Ena/VASP deteriorates lamellipodium architecture in B16-F1 cells, related to ***Figure 6***. Animated visualization of the three-dimensional organization of lamellipodia of B16-F1 wild-type and EVM-KO cells resolved by electron tomography. A

3D model of the actin filament network corresponds to Figure 6A and was obtained by automatic tracking of filaments through the tomogram slices.

Figure 7. Inactivation of Evl in MV^{D7} cells impairs FA formation. (**A**) Spreading of MV^{D7}, EVM-KO and reconstituted cells on fibronectin. EGFP-Evl expressing cell are marked by red asterisks. Time is in minutes. Bar, 25 µm. (**B**) Quantification of cell area over time. Data are means ± SEM. n, number of analyzed cells from 5 independent experiments. (**C**) Quantification of spreading rate. (**D**) Expression of EGFP-tagged Evl, -VASP or -Mena in MVE-KO cells promotes the formation of FA. Immunolabeling of EGFP and vinculin in cells seeded on fibronectin. Bars, 20 µm. (**E**) Representative micrographs of MV^{D7}, MVE-KO and reconstituted cells displaying vinculin staining before *(upper panel*) and after processing by Focal Adhesion Analysis Server (*lower panel*). Bar, 10 µm. (**F**) Quantification of vinculin intensities in FA. (**G**) Quantification of FA size. (**H)** Quantification of FA number per cell. (C and H) *p<0.05, **p<0.01, ***p<0.001 and n.s., not significant by Kruskal-Wallis test and Dunn's Multiple Comparison test or by one-way ANOVA and Tukey Multiple Comparison test (F-G), respectively. n, number of analyzed cells from 3 independent experiments. Boxes in box plots indicate 50% (25-75%) and whiskers (5-95%) of all measurements, with dashed black lines depicting the medians, arithmetic means are highlighted in red.

The following video and figure supplement are available for figure 7:

Figure 7-figure supplement 1. Loss of Ena/VASP proteins affects cell spreading and FA formation in B16-F1 cells. (**A**) Spreading of B16-F1, EVM-KO and reconstituted cells on laminin-coated glass. EGFP-VASP or EGFP-Evl expressing EVM-KO cells are marked by red asterisks. Time is in minutes. Scale bar, 25 µm. (**B**) Quantification of cell area over time. Bars and error bars represent arithmetic means and SEM, respectively. n, number of analyzed

cells from 5 independent experiments. (**C**) Quantification of spreading rate. *p<0.05, **p<0.01, ***p<0.001 and n.s., not significant by Kruskal-Wallis test and Dunn's Multiple Comparison test. n, number of analyzed cells from at least 3 independent experiments.

Figure 7-video 1. Loss of Evl in MV^{D7} cells diminishes spreading on fibronectin, related to ***Figure 7***. MV^{D7}, MVE-KO and reconstituted cells expressing EGFP-Evl were seeded onto fibronectin and recorded by time-lapse phase-contrast imaging using a 20x objective. Reconstituted cells are highlighted by asterisks. Note enhanced spreading in MVE-KO cells expressing EGFP-Evl. Time, min:s. Scale bar, 25 µm.

Figure 8. Confined MVE-KO cells exhibit diminished traction forces. (**A**) Representative micrographs of cells plated on crossbow-shaped polyacrylamide micropatterns coated with fibronectin. MV^{D7} and MVE-KO were stained with CellTracker^{TM} Green and rescued cells were stably expressing EGFP-Evl. Bar, 10 µm. (**B** and **D**) Quantifications of contractile energy of MV^{D7}, MVE-KO and Evl expressing cells plated on crossbow-shaped polyacrylamide micropatterns in independent experiments. ***p<0.001 by Mann-Whitney U rank sum test. n, number of cells analyzed. Boxes in box plots indicate 50% (25-75%) and whiskers (5-95%) of all measurements, with dashed black lines depicting the medians, arithmetic means are highlighted in red. (**C** and **E**) Images depicting averaged traction force field representations of cells indicated. Bar, 10 µm. Force scale bar is in Pascal and arrows represent the local force magnitude and orientation.

The following figure supplement is available for figure 8:

Figure 8-figure supplement 1. Inactivation of Evl in unconfined MV^{D7} cells diminishes cell contractile energy. (**A**) Quantifications of contractile energy normalized by cellular area and

measured for MV^{D7}, MVE-KO and Evl-rescue of MVE-KO cells plated on plain polyacrylamide micropatterns coated with fibronectin. ***p<0.001 or n.s., not significant by Kruskal-Wallis test and Dunn's Multiple Comparison test. n, number of cells analyzed. Boxes in box plots indicate 50% (25-75%) and whiskers (5-95%) of all measurements, with dashed black lines depicting the medians, arithmetic means are highlighted in red. (**B**) Images depicting representative traction force field representations from cells of distinct genotypes, as indicated. Force scale bar is in Pascal and arrows represent local force magnitude and orientation.

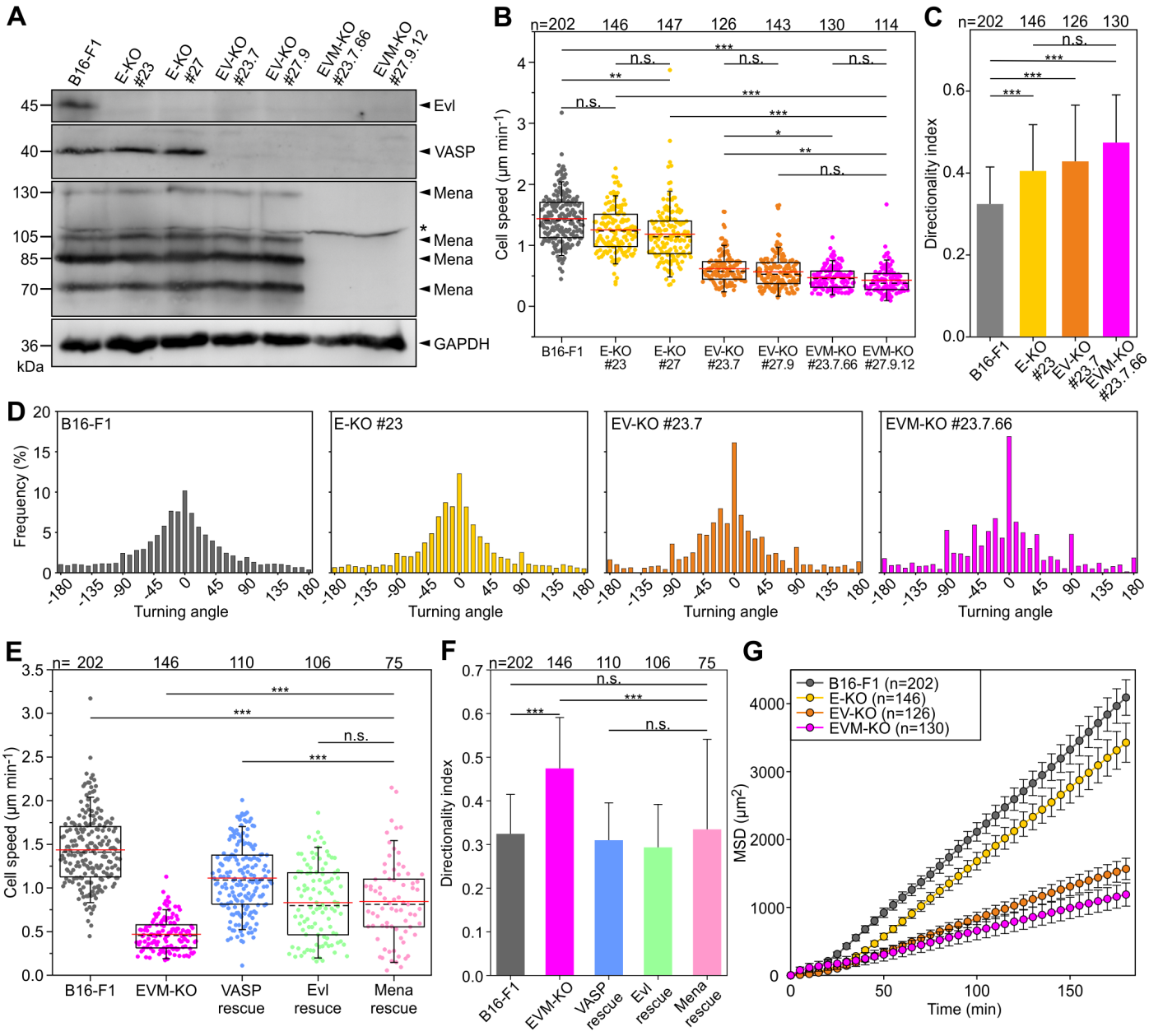
A
B16-F1
E-KO #23
E-KO #27
EV-KO #23.7
EV-KO #27.9
EVM-KO #23.7.66
EVM-KO #27.9.12
45
40
130
105
85
70
36
kDa
Evl
VASP
Mena
*
Mena
Mena
Mena
GAPDH
B
n=202 146 147 126 143 130 114
Cell speed (μm min-1)
n.s.
**
***
*
C
n=202 146 126 130
Directionality index
D
B16-F1
E-KO #23
EV-KO #23.7
EVM-KO #23.7.66
Frequency (%)
Turning angle
E
n= 202 146 110 106 75
Cell speed (μm min-1)
B16-F1
EVM-KO
VASP rescue
Evl resuce
Mena rescue
F
n=202 146 110 106 75
Directionality index
G
B16-F1 (n=202)
E-KO (n=146)
EV-KO (n=126)
EVM-KO (n=130)
MSD (μm2)
Time (min)

Figure 1

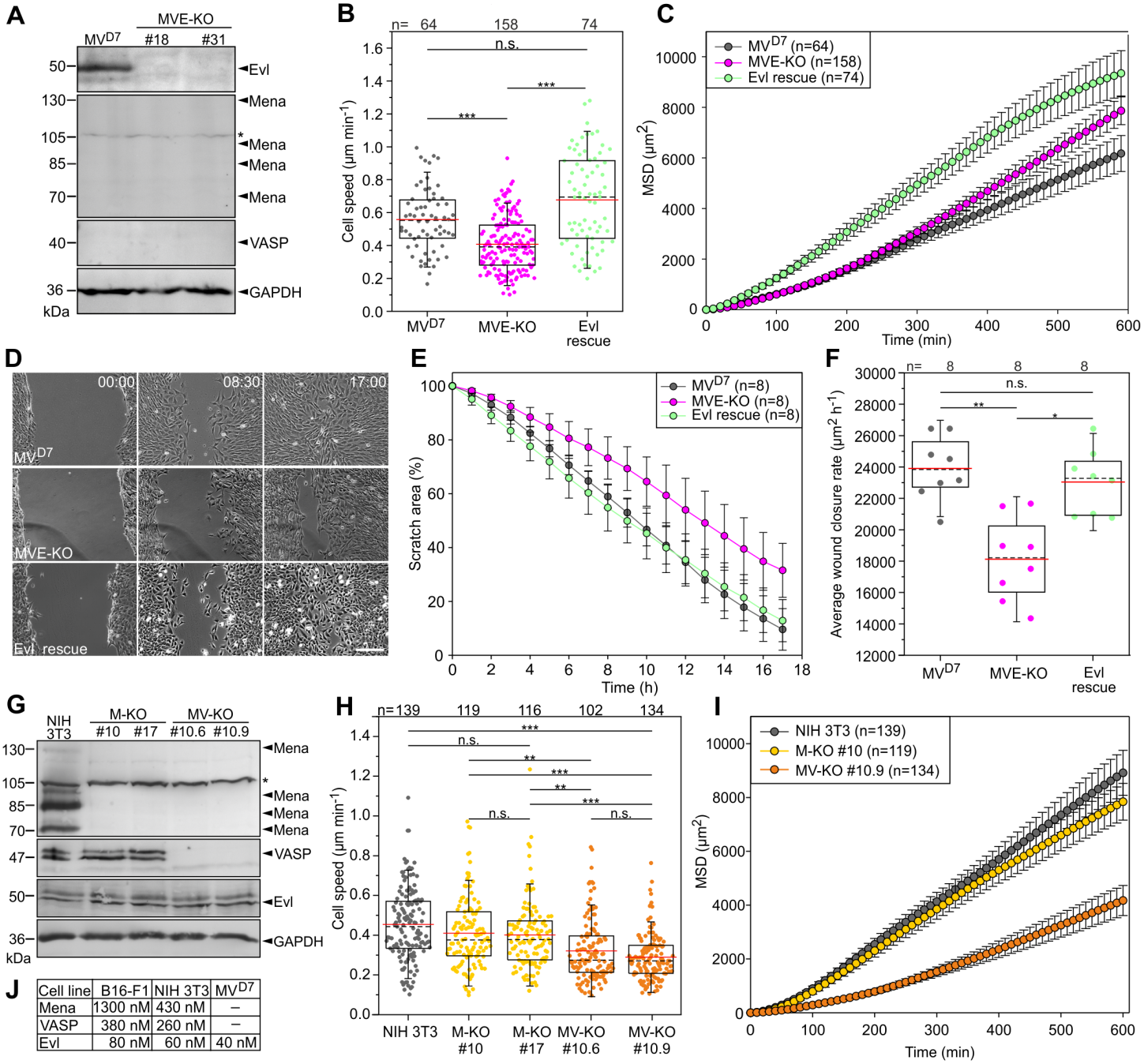

J

Cell line	B16-F1	NIH 3T3	MVD7
Mena	1300 nM	430 nM	–
VASP	380 nM	260 nM	–
Evl	80 nM	60 nM	40 nM

Figure 2

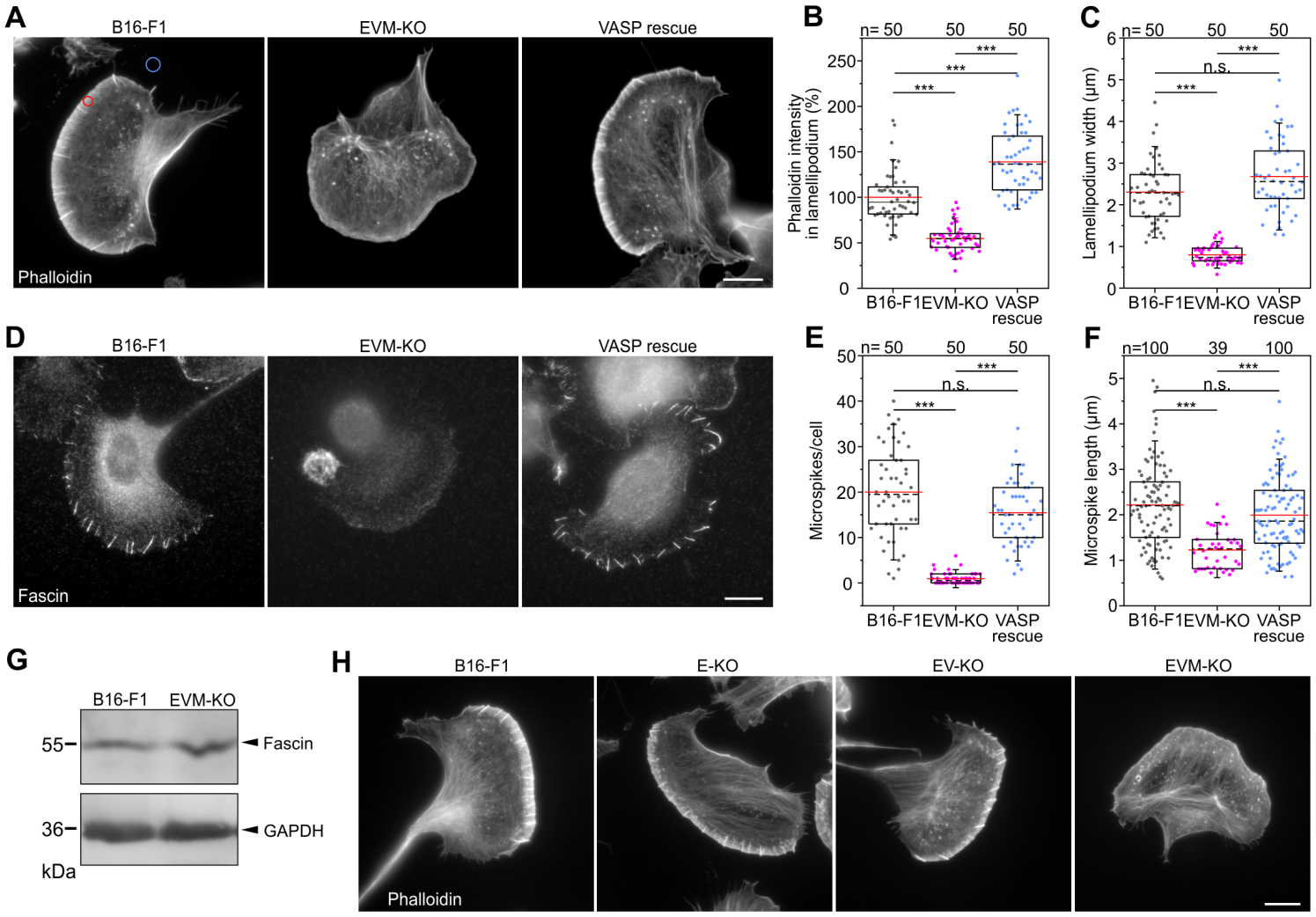
A
B16-F1
EVM-KO
VASP rescue
Phalloidin
B
n= 50 50 50
***
***
***
Phalloidin intensity in lamellipodium (%)
B16-F1 EVM-KO VASP rescue
C
n= 50 50 50
***
n.s.
***
Lamellipodium width (µm)
B16-F1 EVM-KO VASP rescue
D
B16-F1
EVM-KO
VASP rescue
Fascin
E
n= 50 50 50
***
n.s.
***
Microspikes/cell
B16-F1 EVM-KO VASP rescue
F
n=100 39 100
***
n.s.
***
Microspike length (µm)
B16-F1 EVM-KO VASP rescue
G
B16-F1 EVM-KO
55
Fascin
36
GAPDH
kDa
H
B16-F1
E-KO
EV-KO
EVM-KO
Phalloidin

Figure 3

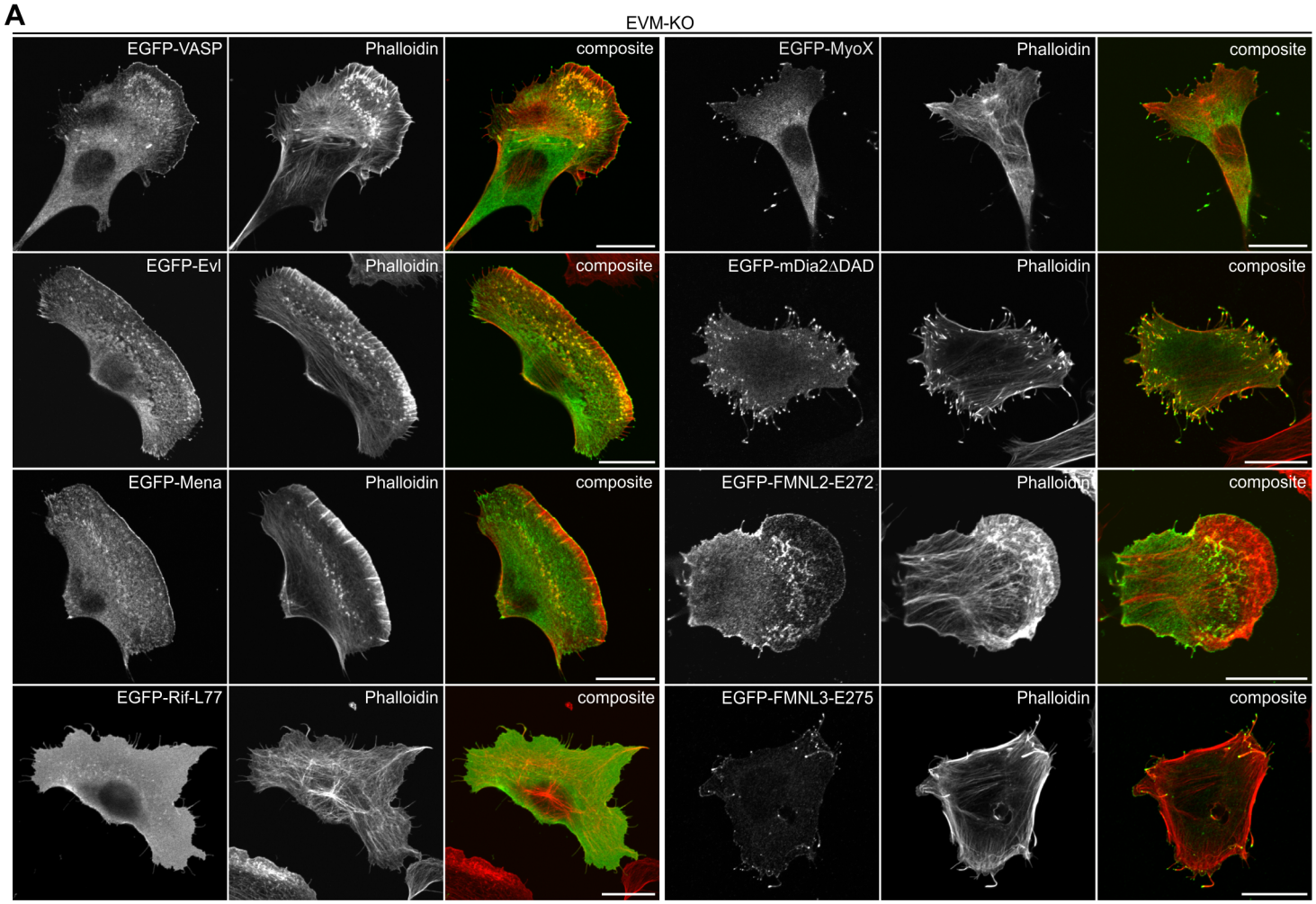
A
EVM-KO
EGFP-VASP
Phalloidin
composite
EGFP-MyoX
Phalloidin
composite
EGFP-Evl
Phalloidin
composite
EGFP-mDia2ΔDAD
Phalloidin
composite
EGFP-Mena
Phalloidin
composite
EGFP-FMNL2-E272
Phalloidin
composite
EGFP-Rif-L77
Phalloidin
composite
EGFP-FMNL3-E275
Phalloidin
composite

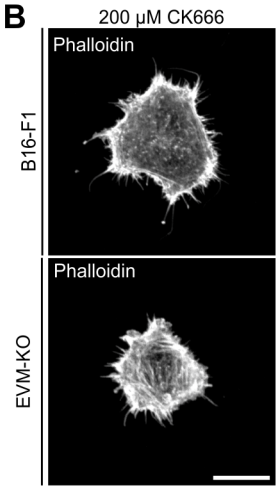
B
200 μM CK666
B16-F1
Phalloidin
EVM-KO
Phalloidin

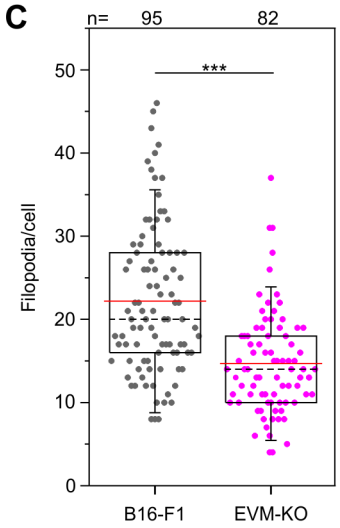
C
n= 95 82
***
Filopodia/cell
0
10
20
30
40
50
B16-F1
EVM-KO

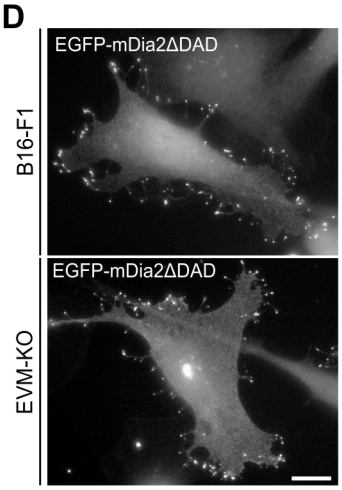
D
B16-F1
EGFP-mDia2ΔDAD
EVM-KO
EGFP-mDia2ΔDAD

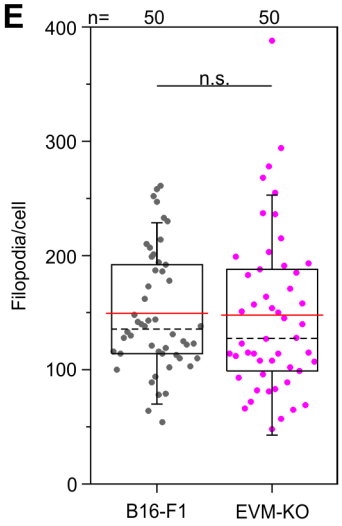
E
n= 50 50
n.s.
Filopodia/cell
0
100
200
300
400
B16-F1
EVM-KO

Figure 4

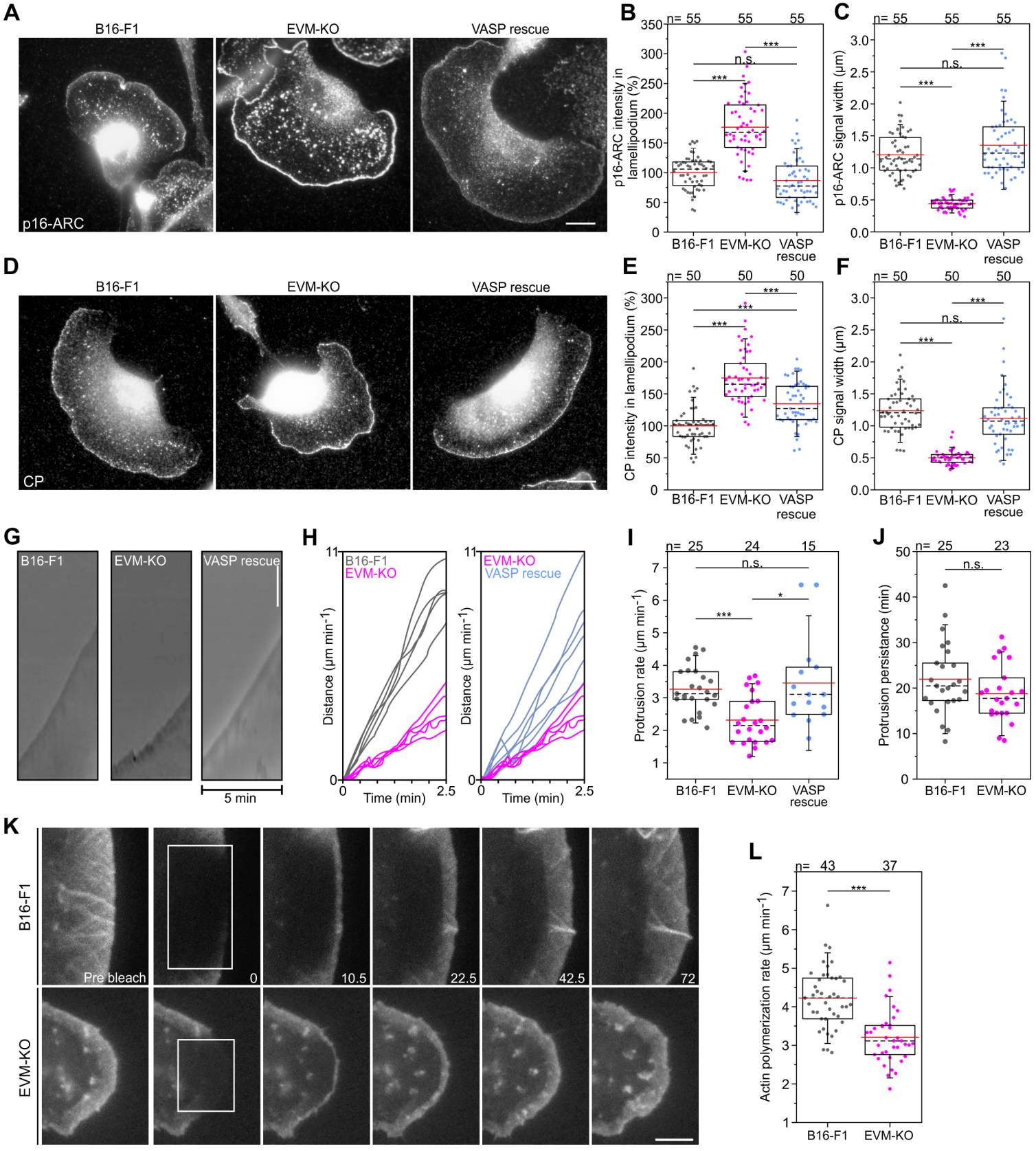
A
B16-F1
EVM-KO
VASP rescue
p16-ARC
B
n= 55 55 55
p16-ARC intensity in lamellipodium (%)
n.s.
***
B16-F1 EVM-KO VASP rescue
C
n= 55 55 55
p16-ARC signal width (μm)
n.s.
***
B16-F1 EVM-KO VASP rescue
D
B16-F1
EVM-KO
VASP rescue
CP
E
n= 50 50 50
CP intensity in lamellipodium (%)
n.s.
***
B16-F1 EVM-KO VASP rescue
F
n= 50 50 50
CP signal width (μm)
n.s.
***
B16-F1 EVM-KO VASP rescue
G
B16-F1
EVM-KO
VASP rescue
5 min
H
B16-F1
EVM-KO
EVM-KO
VASP rescue
Distance (μm min-1)
Time (min)
I
n= 25 24 15
Protrusion rate (μm min-1)
n.s.
*
***
B16-F1 EVM-KO VASP rescue
J
n= 25 23
Protrusion persistance (min)
n.s.
B16-F1 EVM-KO
K
B16-F1
EVM-KO
Pre bleach
0
10.5
22.5
42.5
72
L
n= 43 37
Actin polymerization rate (μm min-1)
***
B16-F1 EVM-KO

Figure 5

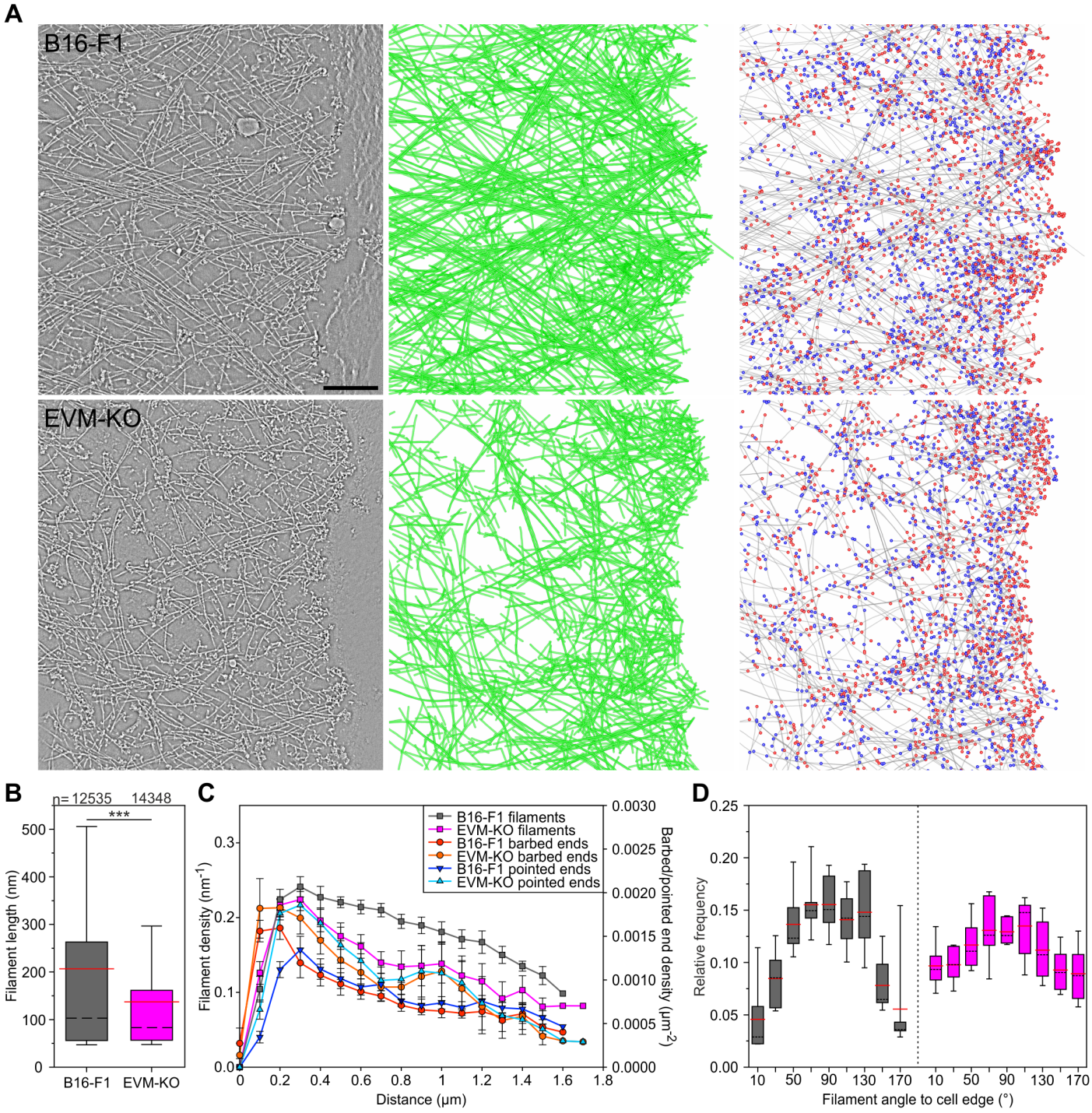
A
B16-F1
EVM-KO
B
n= 12535 14348
***
Filament length (nm)
B16-F1
EVM-KO
C
B16-F1 filaments
EVM-KO filaments
B16-F1 barbed ends
EVM-KO barbed ends
B16-F1 pointed ends
EVM-KO pointed ends
Filament density (nm-1)
Barbed/pointed end density (μm-2)
Distance (μm)
D
Relative frequency
Filament angle to cell edge (°)

Figure 6

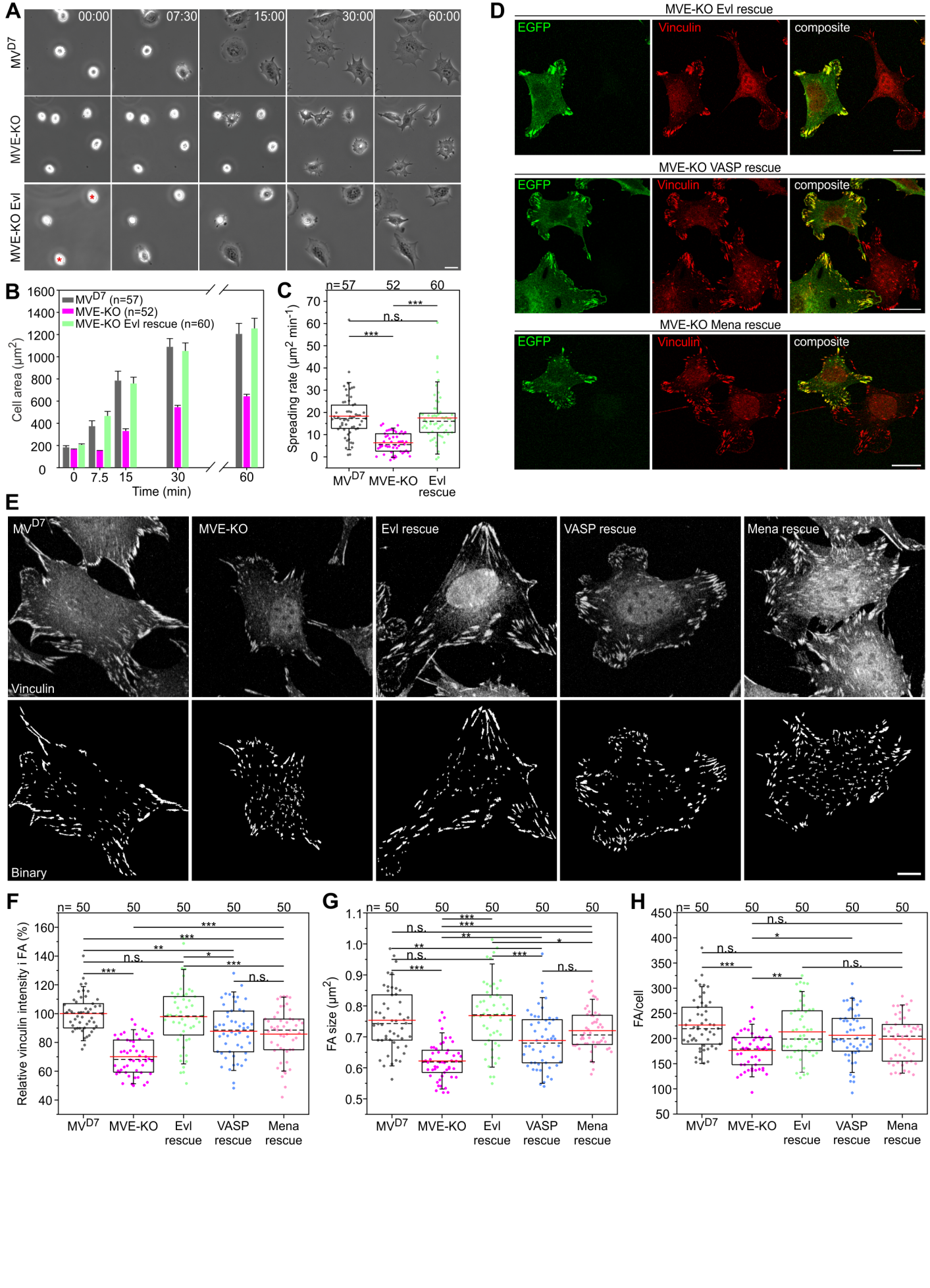
A
00:00
07:30
15:00
30:00
60:00
MVD7
MVE-KO
MVE-KO Evl
B
MVD7 (n=57)
MVE-KO (n=52)
MVE-KO Evl rescue (n=60)
Cell area (µm2)
Time (min)
C
n=57 52 60
Spreading rate (µm2 min-1)
n.s.
MVD7
MVE-KO
Evl rescue
D
MVE-KO Evl rescue
MVE-KO VASP rescue
MVE-KO Mena rescue
EGFP
Vinculin
composite
E
MVD7
MVE-KO
Evl rescue
VASP rescue
Mena rescue
Vinculin
Binary
F
Relative vinculin intensity i FA (%)
n= 50 50 50 50 50
n.s.
MVD7
MVE-KO
Evl rescue
VASP rescue
Mena rescue
G
FA size (µm2)
n= 50 50 50 50 50
n.s.
H
FA/cell
n= 50 50 50 50 50
n.s.

Figure 7

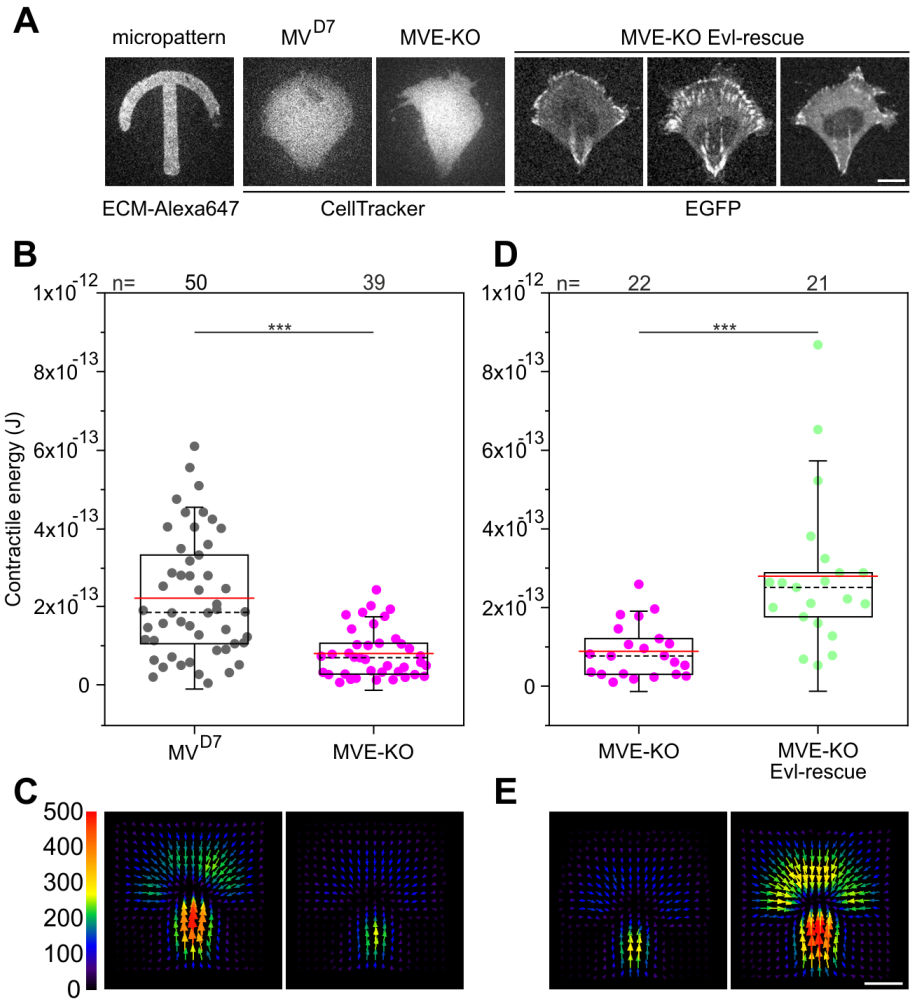
A
micropattern
MV D7
MVE-KO
MVE-KO Evl-rescue
ECM-Alexa647
CellTracker
EGFP
B
n= 50 39
***
Contractile energy (J)
1x10-12
8x10-13
6x10-13
4x10-13
2x10-13
0
MV D7
MVE-KO
D
n= 22 21
***
MVE-KO
MVE-KO Evl-rescue
C
500
400
300
200
100
0
E

Figure 8

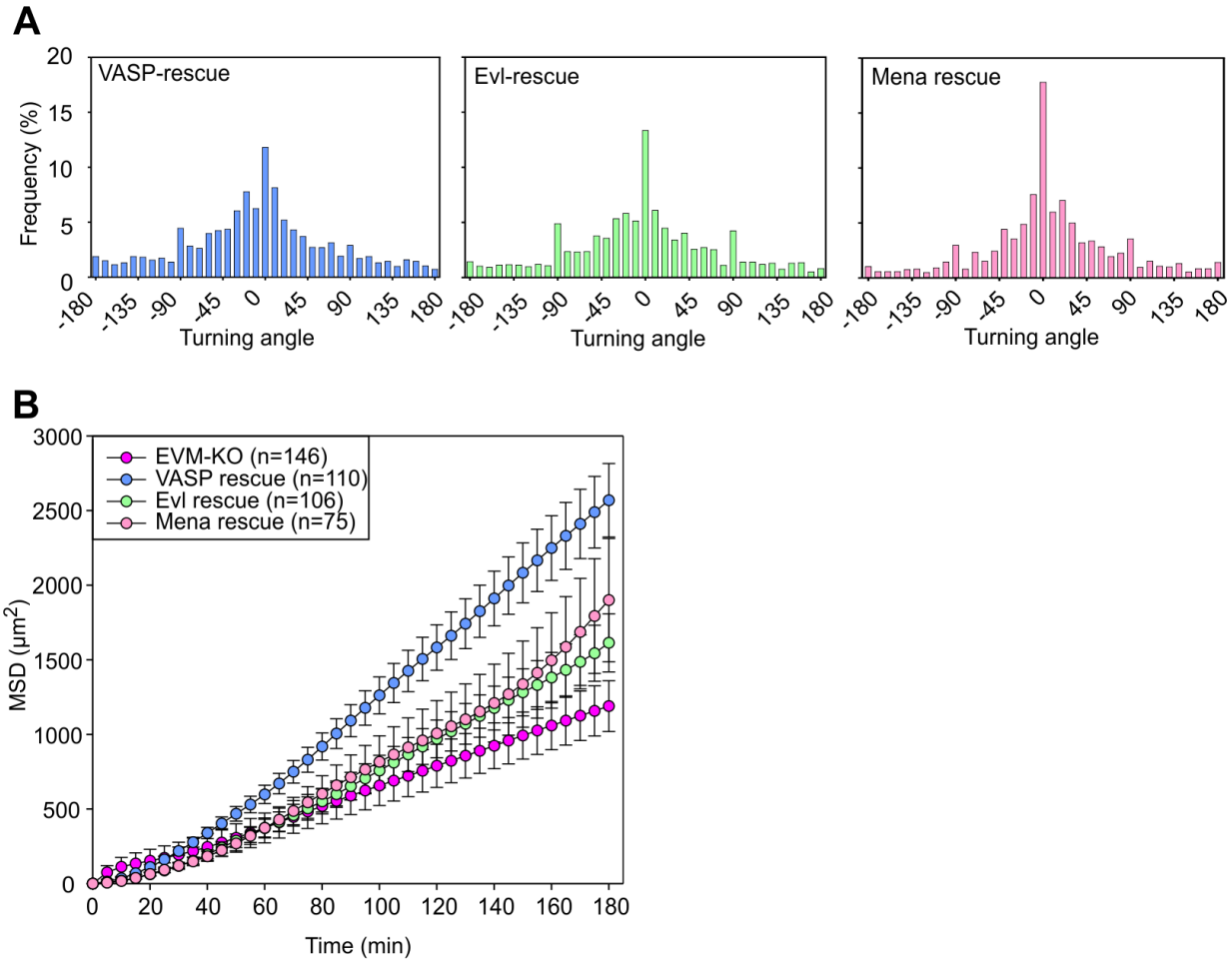

Figure 1-figure supplement 1

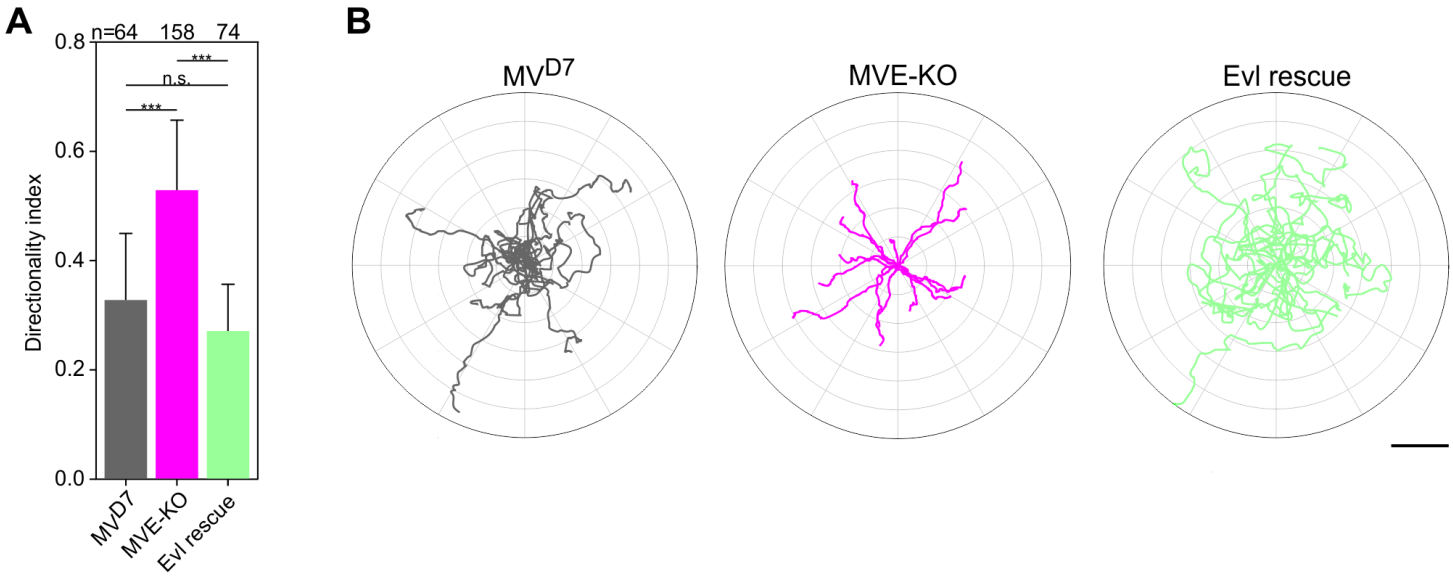

Figure 2-figure supplement 1

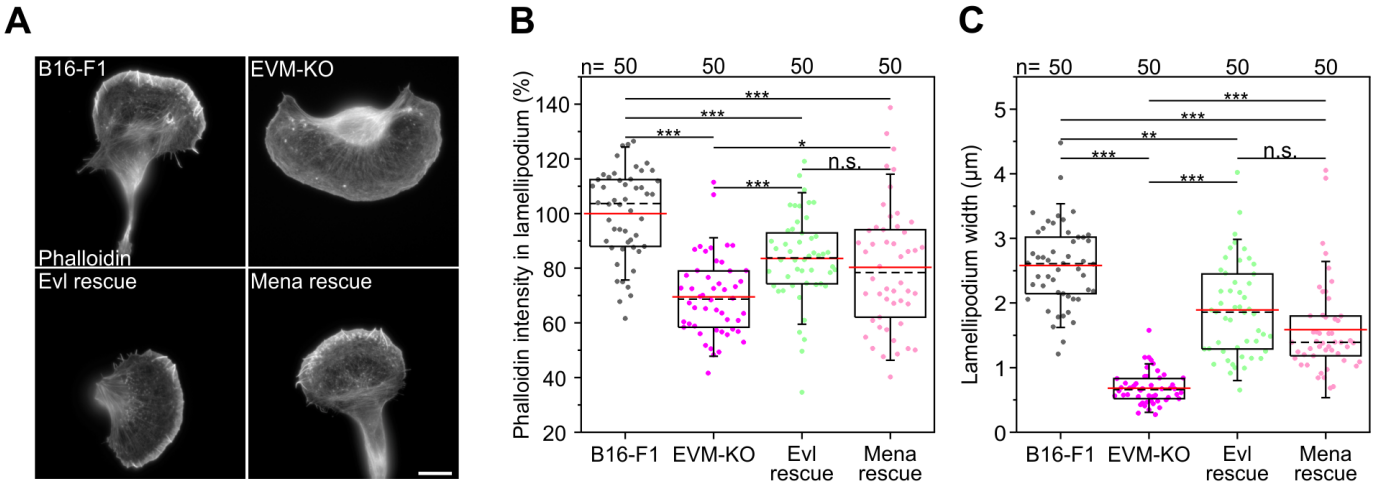

Figure 3-figure supplement 1

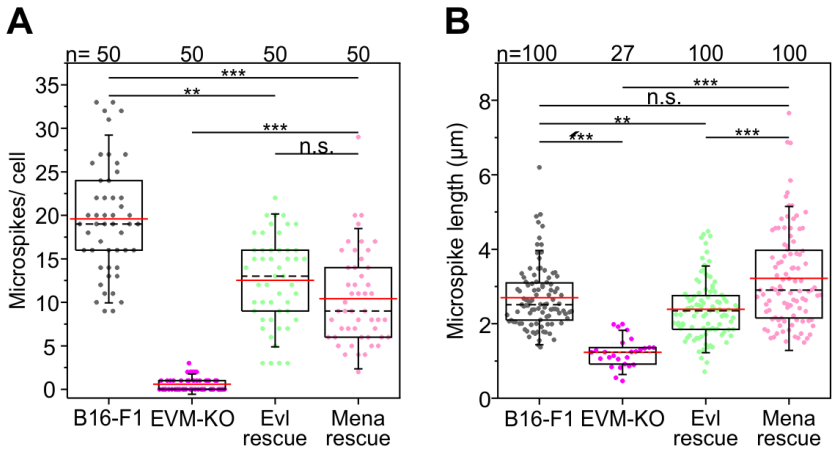

Figure 4-figure supplement 1

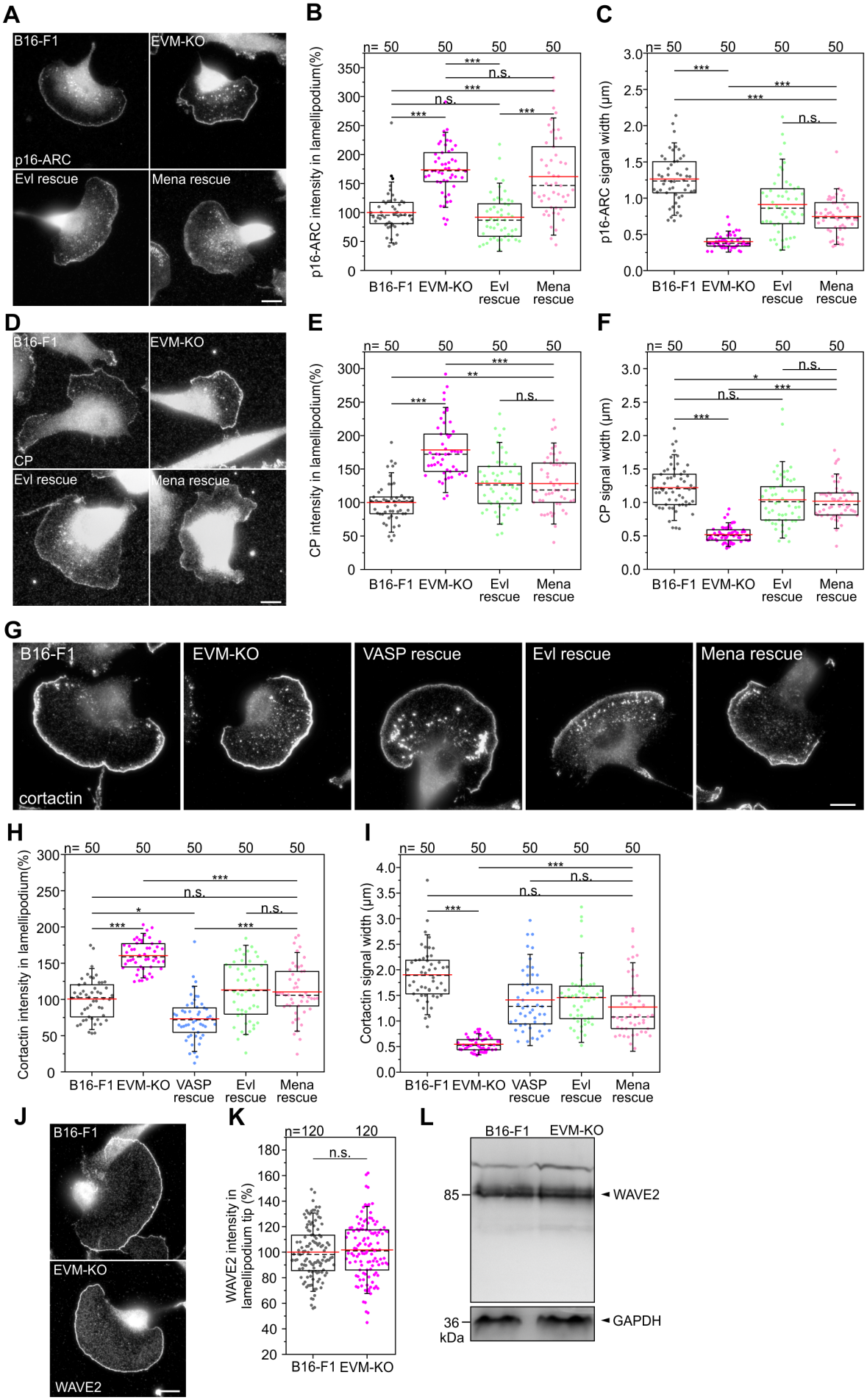

Figure 5-figure supplement 1

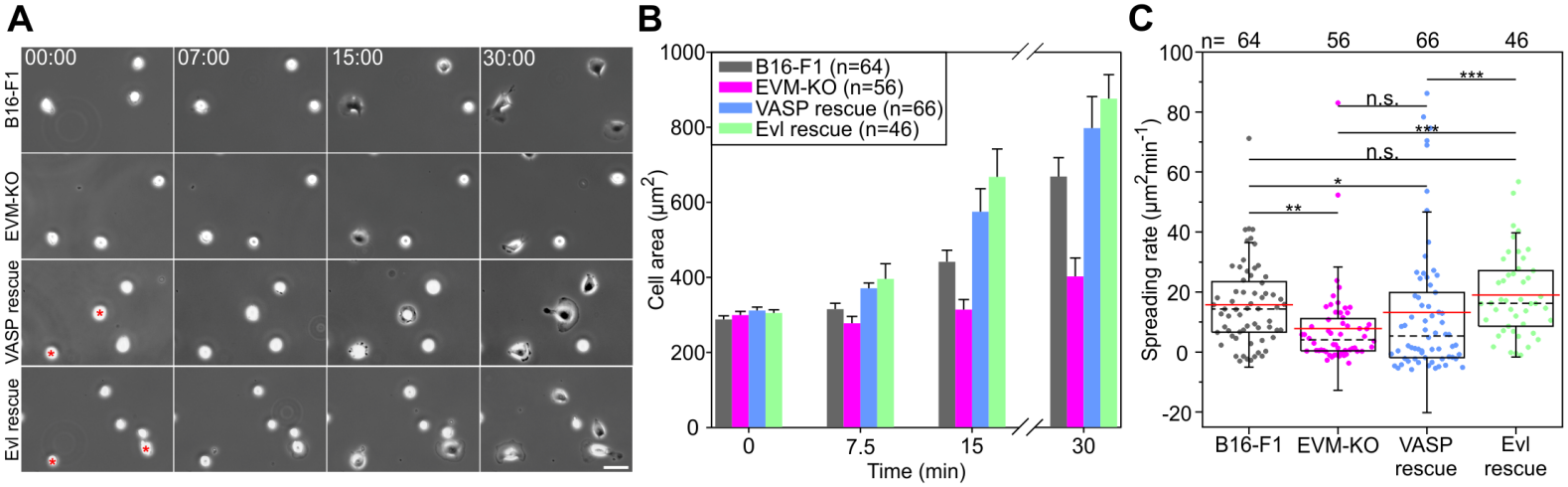

Figure 7-figure supplement 1

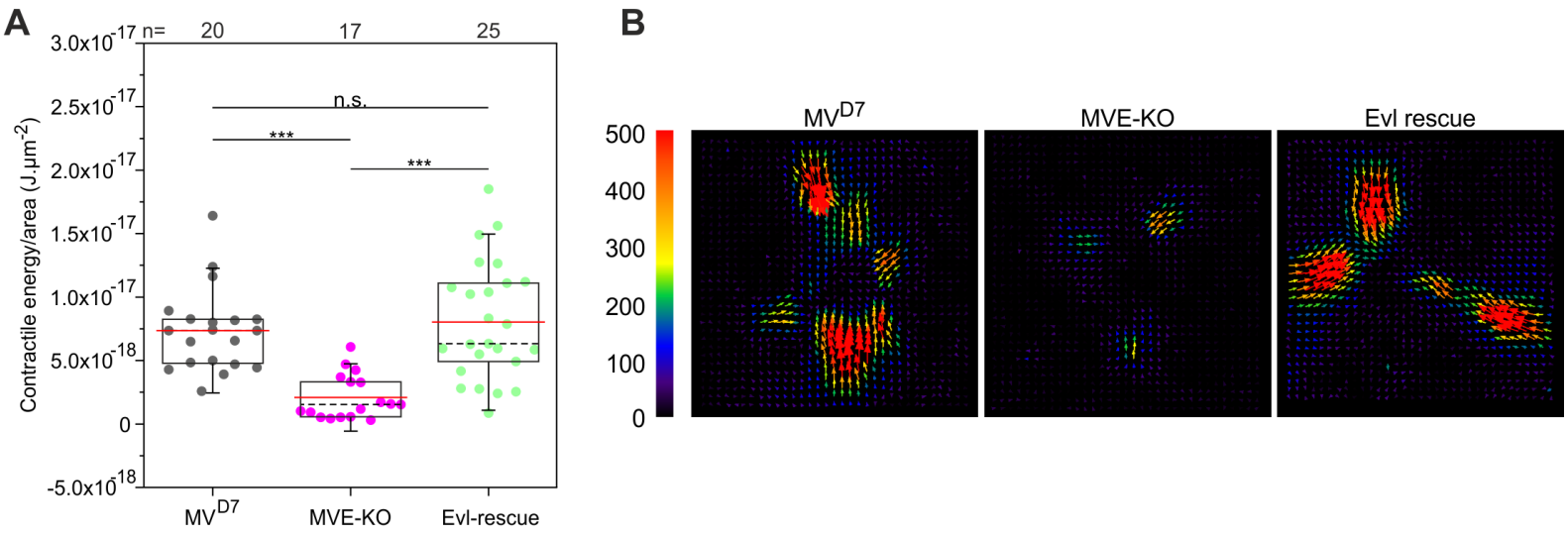

Figure 8-figure supplement 1